

Superrotation and Jet Migration in Simulations of Jupiter’s Convective Zone and Weather Layer

LOREN I. MATILSKY,^{1,*} GEOFFREY K. VALLIS,² MATTHEW K. BROWNING,³ AND NICHOLAS H. BRUMMELL¹

¹*Department of Applied Mathematics, Baskin School of Engineering, University of California, Santa Cruz, CA 95064-1077, USA*

²*Department of Mathematics and Statistics, University of Exeter, Exeter, EX4 4QF, UK*

³*Department of Physics and Astronomy, University of Exeter, Exeter, EX4 4QL, UK*

ABSTRACT

The mean zonal flow observed on Jupiter consists of an intricate pattern of jets, or bands of zonal flow moving prograde or retrograde compared to the bulk planetary rotation. The strongest flow is a superrotating (prograde) jet near the equator, which is flanked by 6–7 retrograde/prograde pairs of weaker jets per hemisphere. The two primary drivers of Jupiter’s zonal flows are thought to be “shallow” baroclinically driven quasi-two-dimensional turbulence in an outer, stably stratified weather layer (WL) and “deep” rotationally constrained buoyantly driven three-dimensional Busse columns in the convective zone (CZ) just underneath the WL. To study both driving mechanisms simultaneously, we implement two rotating, three-dimensional, spherical-shell, anelastic convection simulations of a Jovian-like planet. In one case, the CZ is isolated, whereas in the other case, the upflows are allowed to overshoot into a stably stratified near-surface region, representing an idealized weather layer. We find that in both cases, homogenization of potential vorticity (whose forms in the CZ and WL are distinct) initially creates multiple jets at high latitudes, whereas angular momentum transport by Busse columns drives equatorial superrotation at low latitudes. The presence of an idealized WL significantly alters the thermal wind balance, resulting in large deviations of the meridional contours of the zonal flow from alignment with the rotation axis. Although the superrotation remains stable, the weaker high-latitude jets slowly migrate poleward and/or merge on a very long time scale ($O(10)$ diffusion time scales or thousands of eddy turnover times).

Keywords: Jupiter (873) — Solar system planets (1260) — Planetary science (1255) — Planetary dynamics (2173) — Planetary atmospheres (1244) — Planetary structure (1256)

1. INTRODUCTION

The aim of this paper is to explore how zonal flows arise in simulations of a gas-giant planet like Jupiter, focusing specifically on the comparison between two-dimensional (2D) and three-dimensional (3D) ideas. We seek to build upon previous work over the last few decades on modeling Jupiter’s observed zonal flows, which has typically been performed in either a fully 2D or a fully 3D context. To move towards unification of the various 2D and 3D concepts, we perform fully nonlinear, 3D simulations of a Jovian-like planet and quantitatively assess the results using quasi-2D methods. Here, we first frame the problem by outlining prior observational and theoretical work on Jupiter’s zonal flows. We place par-

ticular emphasis on the role of potential vorticity and the distinct types of turbulent eddies that are thought to dominate the dynamics at different depths of the Jovian interior.

1.1. Superrotation and Jets in Planetary Atmospheres

Mean (longitudinally averaged) zonal flows are a ubiquitous feature of planetary atmospheres. Superrotation—formally defined as a ring of fluid with greater specific angular momentum than that of the planet itself at the equator—is a common property of such zonal flows that appear on the bodies within our solar system (e.g., T. Imamura et al. 2020; G. K. Vallis et al. 2026). For the purposes of the present study, superrotation (or subrotation) can be thought of simply as mean equatorial zonal flow that moves prograde (or retrograde) relative to the bulk planetary rotation. The key parameter determining the nature of zonal flows is thought to be the well-known Rossby number Ro ,

Email: loren.matilsky@gmail.com

* U.S. National Science Foundation
Astronomy and Astrophysics Postdoctoral Fellow

which we here define as¹

$$\text{Ro} := \frac{\text{Rotation time}}{\text{Eddy turnover time}}. \quad (1)$$

For high Rossby numbers, the eddy turnover time is relatively rapid and the eddies do not “feel” the rotation very much; the converse is true for low Rossby numbers. The Rossby number thus measures the influence of rotation on the turbulent eddies, or “rotational constraint.” Both rapidly rotating bodies with $\text{Ro} \ll 1$ /high rotational constraint (like Jupiter and Saturn) and slowly rotating bodies with $\text{Ro} \gg 1$ /low rotational constraint (like Venus and Titan) exhibit permanent strong superrotation (e.g., [P. L. Read & S. Lebonnois 2018](#); [Q. Nicolas & G. K. Vallis 2026](#)). The Sun (about mid-way between fast and slow rotation with $\text{Ro} \sim 1$; e.g., [S. M. Hanasoge et al. 2012](#); [B. J. Greer et al. 2016](#)) also exhibits strong superrotation, with equatorial regions rotating $\sim 10\%$ faster than the bulk rotation rate of the deep solar interior (e.g., [R. Howe 2009](#)). Other planets, like Mars and Earth ($\text{Ro} \sim 0.1\text{--}0.2$), have only a weak and highly variable tendency toward superrotation (e.g., [A. S. Medvedev et al. 2011](#); [G. K. Vallis 2017](#)), whereas Neptune and Uranus ($\text{Ro} \ll 1$) exhibit permanent subrotation (e.g., [D. Soyuer et al. 2022](#)). Observations of superrotation or subrotation on exoplanets is naturally very difficult, however there is evidence that the hottest region of some exoplanet atmospheres is offset eastward from the substellar point (i.e., the point on the planet where the host star is directly overhead), which likely indicates superrotation (e.g., [H. A. Knutson et al. 2007](#); [K. Heng & A. P. Showman 2015](#)). In some cases, superrotation on tidally locked exoplanets has been measured directly using transmission spectroscopy (e.g., [M. Brogi et al. 2016](#); [X. Song & J. Yang 2021](#)).

In addition to superrotation/subrotation, multiple jets—meridionally localized bands of strong zonal flow, often alternating between retrograde and prograde—are observed on Jupiter and Saturn (e.g., [L. N. Fletcher et al. 2020](#); [Y. Kaspi et al. 2020](#)). Jupiter has 6–7 prograde/retrograde jet pairs in each hemisphere (about 25–30 jets total), whereas Saturn has 4–5 pairs of jets per hemisphere (about 15–20 total). On each planet, the most prominent feature is a large superrotating jet straddling the equator.

Understanding the generation of atmospheric zonal flows, especially superrotation/subrotation and jets, is essential for developing a general theory of the wide

range of possible planetary environments. These flows are associated with heat transport, wave generation, shear instabilities, and large-scale overturning circulation. Furthermore, the mechanisms generating atmospheric zonal flows are likely related in a fundamental way to those producing deep “differential rotation” (i.e., shear in the zonal flow), which is thought to be a primary ingredient for producing planetary and stellar magnetic fields through dynamo action (e.g., [E. N. Parker 1993](#); [P. H. Roberts & G. A. Glatzmaier 2000](#)).

1.2. *Jupiter’s Energy Sources*

In this work, we focus on zonal flow generation in a Jovian-like planet of radius $a := 70,000$ km and strong rotational constraint ($\text{Ro} \ll 1$). Jupiter is a particularly interesting system because it has two roughly equal energy sources of free thermal energy that can be tapped to produce the zonal flow. The first is from radiation by the Sun, corresponding to an absorbed energy flux of about 8.2 W m^{-2} , which occurs in the relatively shallow (~ 100 km deep) weather layer (WL). The WL corresponds to the directly observable topmost layers of Jupiter’s interior/atmosphere, which contain several types of clouds and long-lived storms like the Great Red Spot (e.g., [P. S. Marcus 1988](#)). The WL is strongly stable to convection or stably stratified, as inferred from atmospheric temperature profiles obtained by occultation measurements from the Voyager Spacecraft ([G. F. Lindal et al. 1981](#)) and in-situ measurements at one latitude/longitude from the Galileo Probe ([A. Seiff et al. 1996](#)). Because the solar heating is strongest near Jupiter’s equator, this “shallow” energy source induces a pole-to-equator temperature gradient and drives baroclinic eddies. The associated turbulence is quasi-2D because of the stable stratification. The second energy source is a combined effect of Jupiter’s gravitational contraction, precipitation and settling of helium, and internal heat release (i.e., bulk planetary cooling). These effects lead to an outward energy flux of about 7.5 W m^{-2} from the Jovian interior (e.g., [J. Li 2018](#)). This “deep” energy source heats the outer layers of Jupiter from below and drives overturning 3D eddies (often in the form of columnar rolls parallel to the rotation axis owing to the strong rotational constraint) in a roughly 3,000 km-thick convective zone (CZ).

Figure 1 shows a schematic of Jupiter’s interior outer layers (not to scale) from an inner radius r_{in} to an outer radius $r_{\text{out}} := a$. There is a CZ (with its deep rotationally aligned columnar eddies or “Busse columns”; e.g., [F. H. Busse 2002](#)) beneath a WL (with its shallow vertically constricted “pancake eddies” of predominantly horizontal motion), with the boundary between CZ and

¹ Throughout this work, we reserve the symbol “:=” for definitions and use “ \equiv ” to mean “equal to [some constant] everywhere and for all time.”

Schematic of simulation domain and eddy types

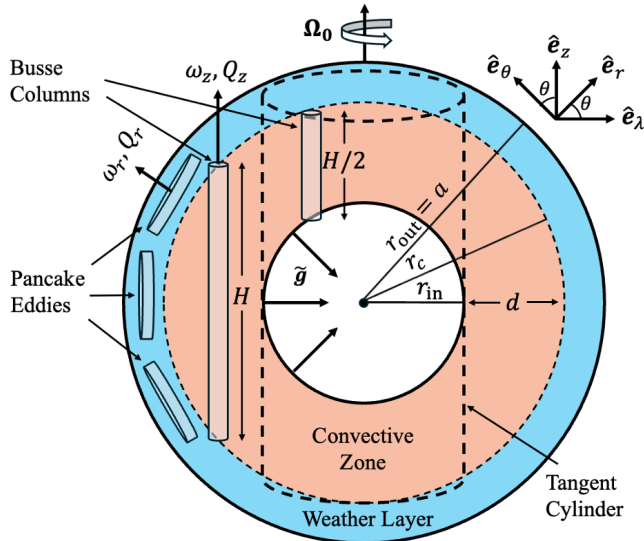


Figure 1. Schematic of our simulation domain (not to scale), showing a spherical shell with a CZ (brown layer) underneath a stably stratified idealized WL (blue layer) with the different types of eddies sketched as rotating cylinders. Each type of eddy mixes a corresponding type of PV: in the CZ, rotationally aligned Busse columns of height $H(\lambda)$ (see Equation 34) mix Q_z (Equation 3), while in the WL, the flattened pancake eddies of primarily horizontal flow mix Q_r (Equation 2). The tangent cylinder, spherical and cylindrical unit vectors, and parameters defined in the text ($r_{\text{in}}, r_c, r_{\text{out}} = a, d = r_c - r_{\text{in}}, \tilde{\mathbf{g}}$, and Ω_0) are also shown.

WL denoted by r_c . We also show the coordinate systems we employ in this work: spherical coordinates ϕ (azimuth angle), θ (latitude), and r (spherical radius) and cylindrical coordinates $\lambda := r \cos \theta$ (cylindrical radius, or moment arm), ϕ , and $z := r \sin \theta$ (axial coordinate). The corresponding unit vectors are denoted with $\hat{\mathbf{e}}$ (for example, the axial unit vector is $\hat{\mathbf{e}}_z$). Note that $(\hat{\mathbf{e}}_\phi, \hat{\mathbf{e}}_\theta, \hat{\mathbf{e}}_r)$ and $(\hat{\mathbf{e}}_\lambda, \hat{\mathbf{e}}_\phi, \hat{\mathbf{e}}_z)$ are both right-handed sets of unit vectors. The system rotates at the frame rate Ω_0 parallel to $\hat{\mathbf{e}}_z$ and feels gravity $\tilde{\mathbf{g}}$ parallel to $-\hat{\mathbf{e}}_r$. The “tangent cylinder” (i.e., the cylinder $\lambda \equiv r_{\text{in}}$ which circumscribes the base of the CZ at $r \equiv r_{\text{in}}$) separates high latitudes (inside the tangent cylinder, where the Busse columns can exist in only one hemisphere or the other) from low latitudes (outside the tangent cylinder, where the columns can extend across the equator).

In ideal circumstances (very strong stratification in the shallow WL and very strong rotational constraint in the deep CZ), we might expect each type of eddy in Figure 1 to be effectively 2D, with the pancake eddies composed of primarily radial vorticity ω_r (which is vertically invariant for a pancake eddy, or independent of r) and the Busse columns composed of primarily axial

vorticity ω_z (which is axially invariant within a column, or independent of z). Here, $\boldsymbol{\omega} := \nabla \times \mathbf{u}$ is the relative vorticity, with \mathbf{u} the fluid velocity measured in the rotating frame. In that case, the equations of motion can be averaged in either r or z to obtain a set of equations similar to those for 2D turbulence. Ideas from 2D turbulence theory can then be used to explain the formation of multiple jets and superrotation.

1.3. Jupiter’s Deep and Shallow Driving Mechanisms for Mean Zonal Flow: Two Types of Potential Vorticity (PV)

Because both types of eddies are effectively 2D in idealized circumstances (because there is symmetry in either r or z), each is thought to drive mean zonal flows according to 2D turbulence theory (e.g., P. B. Rhines 1975). If the origin of the jets is “shallow” (i.e., in the WL), the pancake eddies primarily do the driving, whereas if the origin of the jets is “deep” (i.e., in the CZ), the Busse columns primarily do the driving. This has led to an ongoing “deep versus shallow driving debate” in the community (e.g., G. K. Vallis et al. 2026), and because the energy sources for the different eddy types are roughly equal, the resolution to this debate is not obvious.

Whatever its form (in our case, either pancake eddies or Busse columns), stochastically driven quasi-2D turbulence in a rotating system (angular velocity $\Omega_0 = \Omega_0 \hat{\mathbf{e}}_z$) is thought to drive zonal flows by a turbulent cascade process. Injection of energy at small (rotationally unconstrained) length scales leads to an inverse cascade of energy to larger and larger scales via nonlinear advection (e.g., R. H. Kraichnan 1967). When the eddies become large and slow enough, they begin to feel the effects of rotation and start to take the form of rotationally constrained linear Rossby waves, whose nonlinear interactions (i.e., Reynolds stresses) drive mean zonal flows (e.g., R. E. Dickinson 1969; E. N. Lorenz 1972). The scale at which rotational effects become felt is generally referred to as the Rhines scale (e.g., P. B. Rhines 1975) and simulations of 2D turbulence show that if multiple jets form, they typically each have a width commensurate with the Rhines scale (e.g., G. K. Vallis & M. E. Maltrud 1993; Y. Lian & A. P. Showman 2008). We define the Rhines scale more precisely and make quantitative estimates of it in Sections 4 and 5. Although jet formation from both types of eddy can be described in the context of quasi-2D turbulence and Rhines scales, the different types of symmetry (in either r or z) leads to several differences, most prominently in the distinct forms of the Rhines scale. From symmetry, we also expect jets arising from deep driving (Busse columns) to

be cylindrically aligned (i.e., have z -independent zonal flow), whereas jets arising from shallow driving (pancake eddies) are expected to be vertically aligned (have r -independent zonal flow). Measurements of Jupiter’s gravity field by the Juno Spacecraft have been argued to favor cylindrical alignment of the jets in the CZ (e.g., E. Galanti & Y. Kaspi 2020; Y. Kaspi et al. 2023), but the constraints are not precise enough to give the form of the jets in the WL.

In rotating fluid mechanics, a quantity of key interest is the potential vorticity (PV) of the flow (e.g., C.-G. Rossby 1936; H. Ertel 1942). In many contexts, PV is completely or partially conserved during fluid motion, which results in strong constraints on how global-scale circulations (including circulation in the meridional r - θ plane, as well as mean zonal flows like jets and superrotation) can evolve in a rotating system. In the case of quasi-2D turbulence, PV is often at least partially homogenized on length scales smaller than the Rhines scale. This can lead to a “staircase” in mean PV with respect to latitude θ (for shallow driving) or moment arm λ (for deep driving), for which mean PV is roughly constant on “steps” (each of width the order of the appropriate Rhines scale) and has sharp gradients between the steps. Because the mean PV is related to the θ - or λ -derivative of mean zonal flow, a staircase in mean PV corresponds to multiple zonal jets. The formation of multiple jets and/or superrotation is thus often described in two apparently distinct ways, which are likely different aspects of the same fundamental mechanism, namely, the nonlinear evolution of rotating, quasi-2D turbulence (e.g., G. K. Vallis et al. 2026). One description is in terms of Reynolds stresses from Rossby waves (for scales bigger than the Rhines scale), whereas the other description is in terms of PV staircases from PV homogenization (for scales smaller than the Rhines scale); the jets generally form *at* the Rhines scale, where the two descriptions overlap.

For vortex tubes, such as the idealized pancake vortices and Busse columns sketched in Figure 1, the PV is typically defined as the absolute vorticity (the planetary vorticity $2\Omega_0\hat{e}_z$ added to the relative vorticity $\boldsymbol{\omega}$) divided by the length of the tube (e.g., G. K. Vallis 2017). For the pancake eddies, however, the vertical motion is minimal and stretching and compression effects can be neglected, so the PV reduces simply to the absolute vorticity. Furthermore, because of the low aspect ratio of the pancake eddies, only the vertical component of the angular velocity, $\Omega_0 \sin \theta$, affects the motion of the fluid via the Coriolis force (e.g., J. Pedlosky 1987). The relevant PV thus only has a component in the vertical

direction (\hat{e}_r) and its scalar form is given by

$$Q_r := \omega_r + f, \quad (2)$$

where $f := 2\Omega_0 \sin \theta$ is the Coriolis parameter or background planetary vorticity (also the background PV in this case, since the lengths of the vortex tubes are irrelevant). The variation of f with latitude ($\beta := (1/a)df/d\theta$) gives rise to the “geometric β -effect,” which determines how Rossby waves propagate in a shallow atmosphere (e.g., C.-G. Rossby 1939; B. Haurwitz 1940) and thus the form of the Rhines scale.

For the Busse columns, stretching and compression effects are significant, because the column height quantity H varies significantly as the columns move about in λ (see Figure 1). Furthermore, symmetry of the structures in z does not allow for any of the components of the Coriolis force to be neglected. From Figure 1, the suggested form of PV for a Busse column only has a component in the axial direction (\hat{e}_z) given by

$$Q_z := \frac{\omega_z + 2\Omega_0}{H} = \frac{\omega_z}{H} + f_{\text{topo}} > 0, \quad (3)$$

where, in analogy to f , $f_{\text{topo}} := 2\Omega_0/H$ is the background planetary PV due to the topography, which here comes from the slopes of the bounding spherical shells. Similarly to the pancake vortices, the variation of the planetary PV f_{topo} with moment arm ($\beta_{\text{topo}} := -Hdf_{\text{topo}}/d\lambda = (2\Omega_0/H)dH/d\lambda$) gives rise to a “topographic β -effect,” which is thought to determine a different Rhines scale and staircase/jet structure in the deep driving case compared to the shallow driving case.²

1.4. *Prior Work on Modeling Zonal Flows and the Goals of the Present Study*

The formation of mean zonal flows has been studied extensively in quasi-2D, mostly focusing on the shallow driving mechanism. G. K. Vallis & M. E. Maltrud 1993 used theory and numerical simulations of 2D flow on the β -plane to show that the β -effect (either geometric or topographic, although with a more general form of topography than the one sketched in Figure 1) naturally led to a cascade of energy to scales commensurate with

² Assuming the form of PV in Equation (3) presupposes that the columns extend all the way through the CZ, which is not in general true if there is significant density stratification across the layer. Strong density stratification leads to yet another form of PV due to the “compressional β -effect” (e.g., T. Gastine & J. Wicht 2012). However, in the models discussed in the present work, the density contrast across the layer is rather small (only a factor of 3 or so) and so we do not consider the compressional β -effect further.

the Rhines scale, as well as staircases in PV and multiple jets. Furthermore, they showed that interactions between Rossby waves led to the formation of anisotropic large-scale flows, where generally the zonal component was the largest. Intuitively, this is because the Coriolis force deflects meridional flow into zonal flow.

Shallow driving, of both multiple jets and superrotation, was explored further using the shallow-water equations on the sphere (e.g., J. Y.-K. Cho & L. M. Polvani 1996; R. K. Scott & L. M. Polvani 2007; A. P. Showman 2007; R. K. Scott & L. M. Polvani 2008; W. H. Schubert et al. 2009; I. Saito & K. Ishioka 2015; E. S. Warnford & P. J. Dellar 2017). This setup allowed for the weak compression and stretching of vortex tubes due to variations in the height of the atmosphere, as well as global-scale variations in the β -parameter. The shallow-water formalism was able to capture effects like finite stable stratification and radiative damping, in which cooling at the top of the atmosphere effectively results in a drag on perturbations to the height. In general, multiple jets were robustly found in these shallow-water models, but the form of the Rossby waves and their interaction, and thus the local structure of the jets and staircases, were found to be strongly latitudinally dependent (e.g., R. K. Scott & L. M. Polvani 2007; W. H. Schubert et al. 2009). In general, superrotation and subrotation of the equatorial jet were equally likely (e.g., J. Y.-K. Cho & L. M. Polvani 1996; A. P. Showman 2007), although the presence of sufficient radiative damping was found to lead preferentially to superrotation (I. Saito & K. Ishioka 2015).

Because of the apparent 3D structure of the Busse columns, the deep driving mechanism has been traditionally studied in 3D (although 2D simulations of the shallow-water equations on a disc, assuming a topographic β -effect of the form implied by Equation 3, were recently explored for the first time by Y. Zeng et al. 2025; this extends the constant topographic β -effect from sloped boundaries explored by N. H. Brummell & J. E. Hart 1993 to curved boundaries). By contrast with the 2D models, superrotation was robustly found in 3D simulations of the full fluid equations in a rotating spherical-shell CZ for sufficiently high rotational constraint (e.g., P. A. Gilman & G. A. Glatzmaier 1981; Y. Yamazaki et al. 2005; T. Gastine et al. 2013; M. H. Heimpel et al. 2022; M. E. Camisassa & N. A. Featherstone 2022). Furthermore, for high levels of both turbulence and rotational constraint, multiple high-latitude jets, in addition to superrotation have been consistently achieved in the 3D simulations. Finally, the effects of simultaneous deep and shallow driving have begun to be explored in 3D by simulating a CZ underneath an

outer stably stratified region which could be regarded as an idealized WL (e.g., M. Heimpel et al. 2015; M. H. Heimpel et al. 2022).

Despite this significant progress, there are several key areas that remain to be explored in the context of the deep versus shallow driving debate. First, none of the 3D simulations that we are aware of have been run to equilibration in the mean zonal flows, where by this we mean that the kinetic energy in the zonal flows is still growing (e.g., S.-i. Takehiro et al. 2024) and/or the latitudinal positions of the jets are still changing (e.g., P. N. Wulff et al. 2022). And indeed, long integrations in time have shown that the multiple high-latitude jets achieved in 3D are unsteady, migrating and/or merging to eventually leave only 1–2 high-latitude jets per hemisphere at late times (S.-i. Takehiro et al. 2024). The actual steady state of the 3D simulations thus appears to be unexplored. Second, there have only been a few explicit connections made between the 3D results and the ideas from 2D turbulence theory. For example, M. H. Heimpel et al. (2022) explored the homogenization of PV and staircase formation inside and outside the tangent cylinder. However, we are not aware of work to identify the appropriate forms of PV in the CZ and WL, or an analysis of the local Rhines scale and its comparison with jet width. Finally, only a handful of 3D simulations have explored the deep and shallow driving mechanisms simultaneously (M. Heimpel et al. 2015; M. H. Heimpel et al. 2022) and the influence of the outer layer of stable stratification was not explicitly quantified.

In this work, we consider two 3D spherical-shell anelastic simulations of rapidly rotating thermally driven convection. In the “CZ-only case,” the CZ is isolated with impenetrable boundaries, whereas in the “CZ–WL case,” the convection can overshoot into a thin, stably stratified layer atop the CZ. We consider this top layer to be an idealized “weather layer.” In this first study, the motion in the WL is not driven by external radiation, but by overshooting convection (i.e., there is no external large-scale baroclinic driving). Our WL is further simplified by considering only a single fluid (i.e., no moist convection or conversions between different molecular species, as might be important in the real Jovian cloud deck; e.g., A. P. Ingersoll et al. 2004). Our setup is designed to address the following three questions:

1. What is the ultimate steady state of typical 3D Jovian jet simulations?
2. What are the forms of PV and Rhines scales appropriate for the CZ, WL, and inside/outside the tangent cylinder? How well does the local jet width match the Rhines scale?

3. What is the influence of an idealized WL? Are the cases with and without an idealized WL significantly different?

In Section 2, we describe the numerical details of the two simulations. In Section 3, we describe the basic flow properties of the simulations, including the alternating zonal jets achieved early in the simulation. We then describe the formation of these jets at early times via PV homogenization separately for the CZ (Section 4) and WL (Section 5). In Section 6, we show that the superrotation outside the tangent cylinder is a direct result of angular momentum transport by Busse columns, but only weakly consistent with homogenization of PV. In Section 7, we describe the slow poleward migration and eventual disappearance of the high-latitude jets. In Section 8, we discuss our results and offer some concluding remarks.

2. NUMERICAL SETUP

We evolve the anelastic fluid equations in 3D, rotating spherical shells using the open-source `Rayleigh` code (N. A. Featherstone & B. W. Hindman 2016; H. Matsui et al. 2016; N. A. Featherstone et al. 2024). `Rayleigh` is pseudospectral, evolving nonlinear terms on the right-hand sides of the equations of motion in physical space (a grid in r , θ , and ϕ) and linear terms in spectral space (a truncated set of Chebyshev basis functions in the radial direction and spherical harmonics in the horizontal directions).

2.1. Simulation Geometry

We consider two spherical-shell simulations in this work. Each shell contains a CZ in the region $r_{\text{in}}^* \leq r^* \leq r_c^*$, where r_{in}^* is the inner boundary of the domain and r_c^* is the top of the CZ (r_{in}^* and r_c^* are shared constants for both simulations).³ In the CZ-only case, there is an isolated CZ and the domain's outer boundary r_{out}^* is equal to r_c^* . The other case contains a stably stratified, idealized WL above the CZ. In this CZ–WL case, $r_{\text{out}}^* > r_c^*$ and the convection is allowed to overshoot across $r^* = r_c^*$ into the WL.

This geometry is characterized by the aspect ratio of the CZ,

$$\alpha_{\text{cz}} := \frac{r_{\text{in}}^*}{r_c^*} \equiv 0.8 \quad (4)$$

³ From this section onward, asterisks denote explicitly dimensional variables while the lack of asterisks denote their nondimensional counterparts. Our chosen nondimensionalization is given in Section 2.4.

and the aspect ratio of the WL,

$$\alpha_{\text{wl}} := \frac{r_c^*}{r_{\text{out}}^*} = \begin{cases} 1 & \text{CZ-only case} \\ 0.952 & \text{CZ–WL case.} \end{cases} \quad (5)$$

We choose the CZ depth $d := r_c^* - r_{\text{in}}^*$ as our unit of length, leading to the following nondimensional radii:

$$r_{\text{in}} := \frac{\alpha_{\text{cz}}}{1 - \alpha_{\text{cz}}} = 4, \quad (6a)$$

$$r_c := \frac{1}{1 - \alpha_{\text{cz}}} = 5, \quad \text{and} \quad (6b)$$

$$r_{\text{out}} := \frac{1}{\alpha_{\text{wl}}(1 - \alpha_{\text{cz}})} = \begin{cases} 5 & \text{CZ-only case} \\ 5.25 & \text{CZ–WL case.} \end{cases} \quad (6c)$$

For $a = 70,000$ km, this results in a unit of length of $d = a/5.25 = 13,000$ km.

2.2. Background State

The anelastic approximation consists of assuming a solenoidal mass flux and thermal perturbations that are small relative to a hydrostatically and thermally balanced background state (e.g., Y. Ogura & N. A. Phillips 1962; D. O. Gough 1969). The background state consists of the background density $\tilde{\rho}^*$, temperature \tilde{T}^* , pressure \tilde{p}^* , gravitational acceleration \tilde{g}^* , buoyancy frequency \tilde{N}^* , prescribed internal heating/cooling \tilde{Q}^* , viscosity $\tilde{\nu}^*$, and thermal diffusivity $\tilde{\kappa}^*$. Ideally, we would choose these profiles based on an accurate Jovian structure model. However, given the inherent uncertainty in these structure models (e.g., T. Guillot 2005; M. French et al. 2012) and the necessarily great separation in parameter space between our simulations and the appropriate astrophysical environment to begin with, we opt for a simpler approach.

This approach is described in detail in Appendix A, but the essential assumptions are as follows. We assume a perfect gas, hydrostatic balance, $\tilde{g}^* \propto 1/r^{*2}$, adiabatic background stratification ($\tilde{N}^* \equiv 0$) in the CZ and stable background stratification ($\tilde{N}^{*2} > 0$) in the WL.

The parameters controlling the background state are then the specific heat ratio

$$\gamma := \frac{c_p}{c_v} \equiv \frac{3}{2} \quad (7)$$

(where the specific heat at constant pressure c_p and the specific heat at constant volume c_v are constants), the number of density scale heights across the CZ,

$$N_{\rho}^{\text{cz}} := \ln \left[\frac{\tilde{\rho}^*(r_{\text{in}}^*)}{\tilde{\rho}^*(r_c^*)} \right] \equiv 1.2 \quad (8)$$

and the number of scale heights across the WL,

$$N_{\rho}^{\text{wl}} := \ln \left[\frac{\tilde{\rho}^*(r_c^*)}{\tilde{\rho}^*(r_{\text{out}}^*)} \right] = 0.530. \quad (9)$$

These choices, along with the geometric parameters α_{cz} and α_{wl} , fully determine the thermal profiles $\tilde{\rho}^*$, \tilde{p}^* , and \tilde{T}^* (see Equations A8 and A10.) In the CZ, these choices result in the polytropic stratification $\tilde{\rho}^* \propto \tilde{T}^{*n}$, where $n := 1/(\gamma - 1) \equiv 2$, which appears to be appropriate for Jupiter (e.g., C. Jones et al. 2011). Note that the dimensional background entropy \tilde{s}^* is given by

$$\left(\frac{d\tilde{s}}{dr}\right)^* = \frac{c_p}{\tilde{g}^*} \tilde{N}^{*2}, \quad (10)$$

where we set the arbitrary integration factor such that $\tilde{s}^* \equiv 0$ in the CZ (see Equations A9 and A12.)

We drive the convection by choosing \tilde{Q}^* to heat the bottom regions of the CZ and cool the top regions in two narrow boundary layers (see Equation A16.) Driving the convection by heating and cooling layers has the advantage of yielding “diffusion-free” scalings for the heat transport in certain regimes (e.g., G. Hadjerci et al. 2024; T. Joshi-Hartley et al. 2025; N. T. Lewis et al. 2026). Physically, \tilde{Q}^* represents the incoming flux from Jupiter’s interior due to effects like gravitational contraction, as well as radiative cooling at the surface. In this first study, we neglect the irradiance from the Sun, which would induce an additional latitudinally varying energy source and associated baroclinicity in the WL. Note that the flux \tilde{F}^* driven through the system via \tilde{Q}^* , which is mostly carried by convection in the steady state, is

$$\tilde{F}^* := \frac{1}{r^{*2}} \int_{r_{\text{in}}^*}^{r^*} \tilde{Q}^*(r') r'^2 dr'. \quad (11)$$

We choose $\tilde{\nu}^* \equiv \nu$ and $\tilde{\kappa}^* \equiv \kappa$ to be constants.

Note that as the heating/cooling layers pump energy into the convection, the CZ becomes slightly superadiabatic due to spherically symmetric deviations in the entropy from the background. For the CZ–WL case, this causes a slight restratification in the WL as well, causing the ultimate top boundary of the CZ to deviate slightly from r_c^* . This deviation is extremely small, however, and we do not consider it further, instead taking r_c^* to be the boundary between CZ and WL.

Each simulation’s control parameters are summarized in Table 1. The parameters of the CZ-only case are chosen such that the simulation is as close as possible to the single CZ-only case considered by P. N. Wulff et al. 2022 (see Fig. 3d from that paper). The CZ–WL case is qualitatively similar to the simulations of M. Heimpel et al. (2015); M. H. Heimpel et al. (2022), who implemented a thin region of stable stratification atop a CZ in a spherical shell by injecting heat at both the top and bottom of the shell. This approach allowed the first study of effects like convective overshoot and the inhibition of vertical motion in the stable layer. The CZ–WL case

considered here differs primarily in that we drive convection in the inner layer via the fixed heating/cooling function and enforce the stable layer with an imposed background stable stratification. This allows the precise control of the location of the boundary between the CZ and stable layer and the magnitude of the stable stratification in the WL. Another key difference is that we include the CZ-only case as a control, which allows us to explicitly isolate the effect of a stably stratified WL on the convection and mean zonal flows.

2.3. Equations of Motion

The anelastic fluid equations are solved in a rotating frame with constant angular velocity $\mathbf{\Omega}_0 = \Omega_0 \hat{e}_z$. The Coriolis force is kept but the oblateness and centrifugal force are ignored. **Rayleigh** computes the evolution with respect to time t^* of the three components of vector velocity $\mathbf{u}^* = u_\phi^* \hat{e}_\phi + u_\theta^* \hat{e}_\theta + u_r^* \hat{e}_r$ ($= u_\lambda^* \hat{e}_\lambda + u_\phi^* \hat{e}_\phi + u_z^* \hat{e}_z$) and the thermal perturbations \hat{p}^* and \hat{s}^* , where the hats denote deviations of the thermal variables from the corresponding background-state profiles.

The anelastic fluid equations that we use are (e.g., T. Clune et al. 1999)

$$\nabla^* \cdot (\tilde{\rho} \mathbf{u})^* \equiv 0, \quad (12)$$

$$\begin{aligned} \left(\tilde{\rho} \frac{D\mathbf{u}}{Dt}\right)^* &= -2\tilde{\rho}^* \mathbf{\Omega}_0 \times \mathbf{u}^* - \left[\tilde{\rho} \nabla \left(\frac{\hat{p}}{\tilde{\rho}}\right)\right]^* \\ &+ \frac{(\tilde{\rho} \tilde{g} \hat{s})^*}{c_p} \hat{e}_r + \nabla^* \cdot (D_{ij}^* \hat{e}_i \hat{e}_j), \end{aligned} \quad (13a)$$

$$\text{where } D_{ij}^* := \left\{ 2\tilde{\rho} \tilde{\nu} \left[e_{ij} - \frac{1}{3} (\nabla \cdot \mathbf{u}) \delta_{ij} \right] \right\}^* \quad (13b)$$

$$\text{and } c_{ij}^* := \frac{1}{2} \left(\frac{\partial u_i}{\partial x_j} + \frac{\partial u_j}{\partial x_i} \right)^*, \quad (13c)$$

and

$$\begin{aligned} \left(\tilde{\rho} \tilde{T} \frac{D\hat{s}}{Dt}\right)^* &= -c_p \left[\tilde{\rho} \tilde{T} \frac{\tilde{N}^2}{\tilde{g}} u_r \right]^* + \tilde{Q}^* \\ &+ \nabla^* \cdot \left(\tilde{\kappa} \tilde{\rho} \tilde{T} \nabla \hat{s} \right)^* + D_{ij}^* e_{ij}^*. \end{aligned} \quad (14)$$

The indices i and j run over the three directions in a Cartesian coordinate system and repeated indices are summed. Note that in Equation (13a), the diffusion of momentum is “Laplacian,” in that the highest-order term in $\nabla \cdot (D_{ij}^* \hat{e}_i \hat{e}_j)$ is $\nabla^2 \mathbf{u}$. This further differentiates the 3D global simulations from 2D models, wherein “hyperdiffusion” (terms like $-\nabla^4 \mathbf{u}$ or even higher-order) is often employed (e.g., M. E. Maltrud & G. K. Vallis 1991; Y. Lian & A. P. Showman 2008). In Equation (14), the

Table 1. Nondimensional input parameters for both the CZ-only and CZ–WL cases.

Parameter	Definition	CZ-only case	CZ–WL case
α_{cz}	$r_{\text{in}}^*/r_{\text{c}}^*$	0.8	0.8
α_{wl}	$r_{\text{c}}^*/r_{\text{in}}^*$	1	0.952
r_{in}	$\alpha_{\text{cz}}/(1 - \alpha_{\text{cz}})$	4	4
r_{c}	$1/(1 - \alpha_{\text{cz}})$	5	5
r_{out}	$1/[\alpha_{\text{wl}}(1 - \alpha_{\text{cz}})]$	5	5.25
γ	$c_{\text{p}}/c_{\text{v}}$	1.5	1.5
N_{ρ}^{cz}	$\ln[\tilde{\rho}^*(r_{\text{in}}^*)/\tilde{\rho}^*(r_{\text{c}}^*)]$	1.2	1.2
N_{ρ}^{wl}	$\ln[\tilde{\rho}^*(r_{\text{c}}^*)/\tilde{\rho}^*(r_{\text{out}}^*)]$	0	0.530
Di	$g_{\text{cz}}d/c_{\text{p}}T_{\text{cz}}$	0.599	0.599
Pr	ν/κ	0.5	0.5
Ra _f	$\frac{g_{\text{cz}}d^3}{\nu\kappa} \frac{\Delta s}{c_{\text{p}}} = \frac{F_{\text{cz}}g_{\text{cz}}d^4}{\rho_{\text{cz}}T_{\text{cz}}c_{\text{p}}\nu\kappa^2}$	10^7	10^7
Ro _c	$\sqrt{g_{\text{cz}}(\Delta s/c_{\text{p}})}/2\Omega_0$	0.2	0.2
Ek	$\nu/4d\Omega_0^2$	4.47×10^{-5}	4.47×10^{-5}
σ	$(N_{\text{wl}}/2\Omega_0)\sqrt{\nu/\kappa}$	-	2.93
Bu	$(N_{\text{wl}}/2\Omega_0)^2$	-	17.2
N_{ϕ}	Number of longitudinal grid points	1536	2304
N_{θ}	Number of latitudinal grid points	768	1152
N_r	Number radial grid points	96	(96, 32)

diffusion of heat, which is also Laplacian, is assumed to respond to entropy gradients instead of temperature gradients, in accordance with mixing-length theory (e.g., [P. A. Gilman 1972](#)).

2.4. Nondimensionalization

We nondimensionalize the coordinates and fields using the following system of units:

$$[\nabla^*] = d^{-1} \quad (15a)$$

$$[\partial/\partial t^*] = 2\Omega_0 \quad (15b)$$

$$[\mathbf{u}^*] = 2\Omega_0 d \quad (15c)$$

$$[\hat{p}^*] = \rho_{\text{cz}}(2\Omega_0 d)^2 \quad (15d)$$

$$[\hat{s}^*] = \Delta s_{\text{est}} := \frac{F_{\text{cz}}d}{\rho_{\text{cz}}T_{\text{cz}}\kappa}. \quad (15e)$$

We use the subscripts ‘‘cz’’ or ‘‘wl’’ to denote the volume-average of a quantity over the CZ or WL, respectively. For the background-state quantities, we omit the tildes (for example, ρ_{cz} denotes the volume-average of $\tilde{\rho}^*$ over the CZ). Note that Δs_{est} is the *estimated* entropy difference across the CZ due to the imposed heat flux. The actual entropy difference Δs after the convection has been established is not known a priori and the Rayleigh number derived below is thus flux-based.

We nondimensionalize the background state by scaling $\tilde{\rho}^*$, \tilde{p}^* , \tilde{T}^* , and \tilde{g}^* by their volume-averages over the CZ, \tilde{Q} by F_{cz}/d , and \tilde{N}^* by N_{wl} .

With these scalings, the nondimensional equations of motion are

$$\nabla \cdot (\tilde{\rho}\mathbf{u}) \equiv 0, \quad (16)$$

$$\begin{aligned} \tilde{\rho} \left(\frac{D\mathbf{u}}{Dt} \right) = & -\tilde{\rho}\hat{\mathbf{e}}_z \times \mathbf{u} - \tilde{\rho}\nabla \left(\frac{\hat{p}}{\tilde{\rho}} \right) + \text{Ro}_c^2 \tilde{\rho} \tilde{g} \hat{\mathbf{s}} \hat{\mathbf{e}}_r \\ & + \sqrt{\frac{\text{Pr}}{\text{Ra}_f}} \text{Ro}_c \nabla \cdot (D_{ij} \hat{\mathbf{e}}_i \hat{\mathbf{e}}_j), \end{aligned} \quad (17)$$

and

$$\begin{aligned} \tilde{\rho} \tilde{T} \frac{D\hat{s}}{Dt} = & -\frac{\sigma^2}{\text{PrRo}_c^2} \tilde{\rho} \tilde{T} \frac{\tilde{N}^2}{\tilde{g}} u_r + \frac{\text{Ro}_c}{\sqrt{\text{PrRa}_f}} \tilde{Q} \\ & + \frac{\text{Ro}_c}{\sqrt{\text{PrRa}_f}} \nabla \cdot (\tilde{\rho} \tilde{T} \tilde{\kappa} \nabla \hat{s}) + \sqrt{\frac{\text{Pr}}{\text{Ra}_f}} \frac{\text{Di}}{\text{Ro}_c} D_{ij} e_{ij}. \end{aligned} \quad (18)$$

The nondimensional control parameters appearing in Equations (16)–(18) are

$$\text{Pr} := \frac{\nu}{\kappa} \quad (\text{thermal Prandtl number}), \quad (19a)$$

$$\begin{aligned} \text{Ra}_f := & \frac{g_{\text{cz}}d^3}{\nu\kappa} \left(\frac{\Delta s_{\text{est}}}{c_{\text{p}}} \right) = \frac{F_{\text{cz}}g_{\text{cz}}d^4}{\rho_{\text{cz}}T_{\text{cz}}c_{\text{p}}\nu\kappa^2} \\ & (\text{flux-based Rayleigh number}), \end{aligned} \quad (19b)$$

$$\begin{aligned} \text{Ro}_c := & \frac{\sqrt{(g_{\text{cz}}/d)(\Delta s_{\text{est}}/c_{\text{p}})}}{2\Omega_0} = \text{Ek} \sqrt{\frac{\text{Ra}}{\text{Pr}}} \\ & (\text{convective Rossby number}), \end{aligned} \quad (19c)$$

and

$$\sigma := \left(\frac{N_{rz}}{2\Omega_0} \right) \sqrt{\frac{\nu}{\kappa}} = \sqrt{\text{BuPr}} \quad (\sigma\text{-parameter}), \quad (19d)$$

where in Equations (19c) and (19d) we have implicitly defined the Ekman number

$$\text{Ek} := \frac{\nu}{2\Omega_0 d^2} \quad (20)$$

and the buoyancy number

$$\text{Bu} := \frac{N_{\text{wl}}^2}{4\Omega_0^2}. \quad (21)$$

The five independent parameters in Equations (19) fully characterize the system and we thus treat Ek and Bu as dependent parameters. The dissipation number

$$\text{Di} := \frac{g_{cz}d}{c_p T_{cz}} \equiv 0.599 \quad (22)$$

is not an independent control parameter, but is a property of the background state (see Equation A13).

We report all results in nondimensional form, but we can always consider an equivalent dimensional system by a process outlined in Appendix B. To convert between nondimensional and dimensional results, use Table B1.

2.5. Initial and boundary conditions

Each simulation is initialized from random noise in \hat{s} of amplitude roughly 10^{-3} , with \mathbf{u} and \hat{p} both $\equiv 0$. The convection then develops and we wait for the system to reach a statistically steady state.

At both boundaries, each case is impenetrable, stress-free, and has zero conductive flux:

$$u_r = \frac{\partial}{\partial r} \left(\frac{u_\theta}{r} \right) = \frac{\partial}{\partial r} \left(\frac{u_\phi}{r} \right) = \frac{\partial \hat{s}}{\partial r} \equiv 0. \quad (23)$$

2.6. Notation for averages

We denote instantaneous longitudinal (or zonal) averages of quantities with angular brackets, e.g., $\langle u_\phi \rangle$. Note that for a given field ψ , we often utilize the Reynolds decomposition $\psi = \langle \psi \rangle + \psi'$ and we call $\langle \psi \rangle$ the mean ψ and ψ' the fluctuating ψ . We append the subscript “sph” to the brackets to denote a horizontal average over a spherical surface (e.g., $\langle \hat{s} \rangle_{\text{sph}}$). We append the subscript “v” to indicate an instantaneous volume-average over a domain that will be specified in the text (e.g., $\langle (\mathbf{u}')^2 \rangle_v$, where the averaging might occur over the volume of the CZ). We denote an instantaneous combined longitudinal and axial average (i.e., taking an average of the longitudinally averaged quantity along z at a fixed

λ) by adding a “ z ” subscript (e.g., $\langle u_\phi \rangle_z$). Inside the tangent cylinder, we perform this z -average separately for each hemisphere. Similarly, we denote a combined longitudinal and radial average in the CZ–WL case (i.e., taking an average of a longitudinally averaged quantity along r at a fixed θ , where the radius range is always taken to be $r = r_c$ to $r = r_{\text{out}}$, i.e., over the WL) by appending an “ r ” subscript (e.g., $\langle u_\phi \rangle_r$). Note that the radial average is weighted by r^2 to take into account the variation of the local volume element along a ray at fixed θ . For a combined spatial and temporal average, we append the subscript “ t ” to the averaged quantity (e.g., $\langle u_\phi \rangle_t$ or $\langle u_\phi \rangle_{r,t}$). The specific interval for the temporal average will be noted in the text.

3. INITIAL FLOW STRUCTURES

The mean zonal flow in our simulations takes a very long time to grow and finally reach equilibration. We say that the zonal flow has reached equilibrium if the following requirements are met: (a) the kinetic energy in the mean zonal flow evolves with time in a statistically stationary manner, (b) the latitudinal structure of the zonal flow is not obviously changing (i.e., no migration/merging of the jets), and (c) the right-hand sides of each of the equations of motion are near zero. Figure 2 shows the evolution of the shell-averaged mean zonal kinetic energy $\tilde{\rho} \langle u_\phi \rangle^2 / 2$ during the full run of each simulation. There is initially very rapid growth in the kinetic energy (for example, over the interval $t = (0, 25000)$ highlighted in Figure 2a), followed by very slow secular growth until the kinetic energy curve finally flattens out, roughly at the time t_{eq} . We estimate t_{eq} by eye from the growth curves and separately confirm that requirements (b) and (c) above are met. We find that multiple jets only appear at early times. To make contact with prior global simulations, which were also mostly analyzed at early times before equilibration, we examine each driving mechanism by averaging over the early time interval $t = 5000 \pm 250$ ($= (4750, 5250)$) highlighted in Figure 2(b). In Sections 3.1–6, we analyze this early time interval exclusively.

3.1. Basic flow properties

Figure 3 shows the fluctuating axial vorticity ω'_z at $t = 5000$. There are many thin, cylindrically aligned columns of vorticity, which basically extend throughout the full CZ in each case. On a given spherical surface near the equator, the cross sections of these columns display the canonical outward spiral associated with Busse columns (e.g., F. H. Busse 2002). The flows in the CZ have largely comparable structure in both cases, but in the WL of the CZ–WL case, the flows are clearly larger-

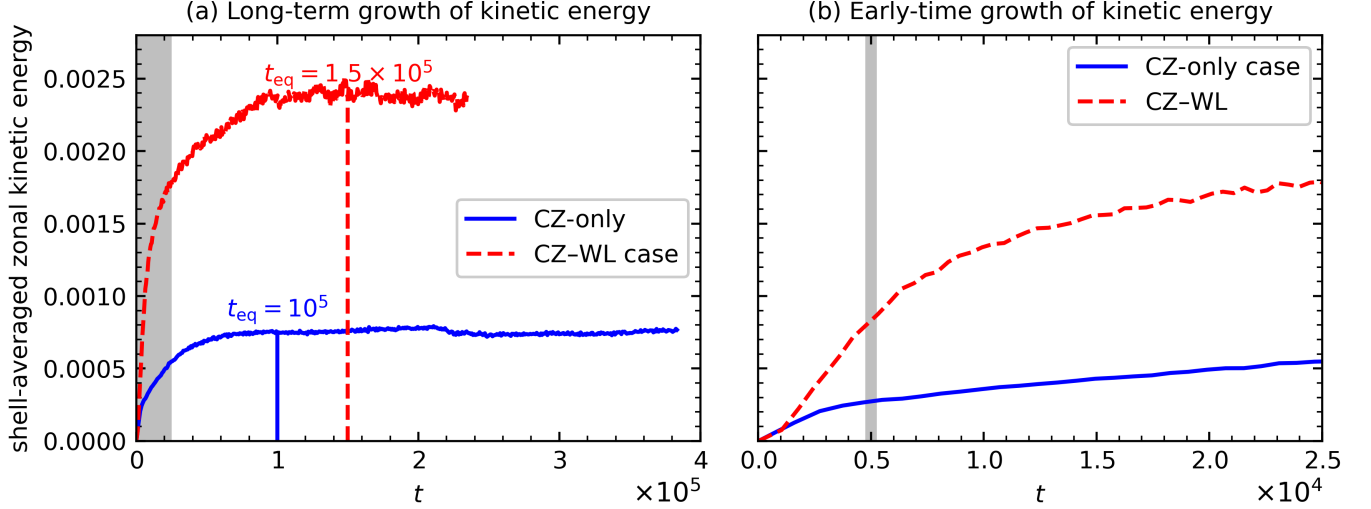


Figure 2. Trace of the mean zonal kinetic energy density, $\tilde{\rho} \langle u_\phi \rangle^2 / 2$, instantaneously volume-averaged over the full shell for each case. (a) Full evolution of the kinetic energy from $t = 0$ to $t = t_{\text{run}}$, with the interval $t = (0, 25000)$ highlighted, and the estimated time at which the simulations finally equilibrate (t_{eq}) labeled by vertical lines. The total run-time of each simulation, t_{run} , is 3.84×10^5 for the CZ-only case and 2.35×10^5 for the CZ-WL case. (b) Early-time evolution of the kinetic energy during the interval $t = (0, 25000)$ highlighted in panel (a). The early-time averaging interval $t = 5000 \pm 250$ analyzed in Sections 3.1–6 is highlighted. Recall that our dimensional unit of time is $(2\Omega_0)^{-1}$ (rotation period divided by 4π) and that in these units, the diffusion timescales are $\text{Ek}^{-1} = 22400$ (viscous) and $\text{Pr}/\text{Ek} = 11200$ (thermal).

Table 2. Nondimensional output parameters for the CZ-only case, the CZ of the CZ-WL case, and the WL of the CZ-WL case. Here the temporal averaging interval is $t = 5000 \pm 250$. See Equations (24)–(27).

Parameter	CZ-only	CZ-WL (CZ)	CZ-WL (WL)
Ro_f	0.19	0.24	0.16
Ro_m	0.087	0.14	0.083
Re_f	180	270	140
Re_m	590	1000	1500
u_f	8.1e-03	0.012	6.1e-03
u_m	0.026	0.045	0.069

scale overall and the symmetry with respect to the rotation axis is broken. Instead, because of the strong stable stratification, the flows in the WL consist of pancake vortices of predominantly horizontal flow with small vertical extent (compare to Figure 1).

Some nondimensional diagnostics characterizing the simulated flows are the Rossby number⁴ of the fluctuating flows, which here we define as

$$\text{Ro}_f := \frac{\langle \langle \omega^{*'} \rangle^2 \rangle_v^{1/2}}{2\Omega_0} = \langle \langle \omega' \rangle^2 \rangle_v^{1/2}, \quad (24)$$

⁴ In this work, we use Equation (1) and identify $(2\Omega_0)^{-1}$ with the rotation time and $|\omega|^{-1}$ with the eddy turnover time.

the Rossby number of the mean flows,

$$\text{Ro}_m := \frac{\langle \langle \omega^* \rangle^2 \rangle_v^{1/2}}{2\Omega_0} = \langle \langle |\omega| \rangle^2 \rangle_v^{1/2}, \quad (25)$$

the Reynolds number of the fluctuating flows,

$$\text{Re}_f := \frac{\langle \langle \mathbf{u}^{*'} \rangle^2 \rangle_v^{1/2} H}{\nu} = \frac{\langle \langle |\mathbf{u}'| \rangle^2 \rangle_v^{1/2}}{\text{Ek}}, \quad (26)$$

the Reynolds number of the mean flows,

$$\text{Re}_m := \frac{\langle \langle \mathbf{u} \rangle^2 \rangle_v^{1/2} H}{\nu} = \frac{\langle \langle \mathbf{u} \rangle^2 \rangle_v^{1/2}}{\text{Ek}}, \quad (27)$$

and the nondimensional amplitudes of the fluctuating and mean flows, which we denote by $u_f := \langle \langle \mathbf{u}' \rangle^2 \rangle_v^{1/2}$ and $u_m := \langle \langle \mathbf{u} \rangle^2 \rangle_v^{1/2}$, respectively. Here, the volume-average is over either the CZ or WL.

Table 2 shows these output parameters separately for each case and region for the interval $t = 5000 \pm 250$. Separate volume-averages are taken for the full shell of the CZ-only case, the CZ of the CZ-WL case, and the WL of the CZ-WL case. All the flows are rotationally constrained, with the various Rossby numbers never exceeding 0.24. The simulations are still reasonably turbulent (even in the WL of the CZ-WL case), with the

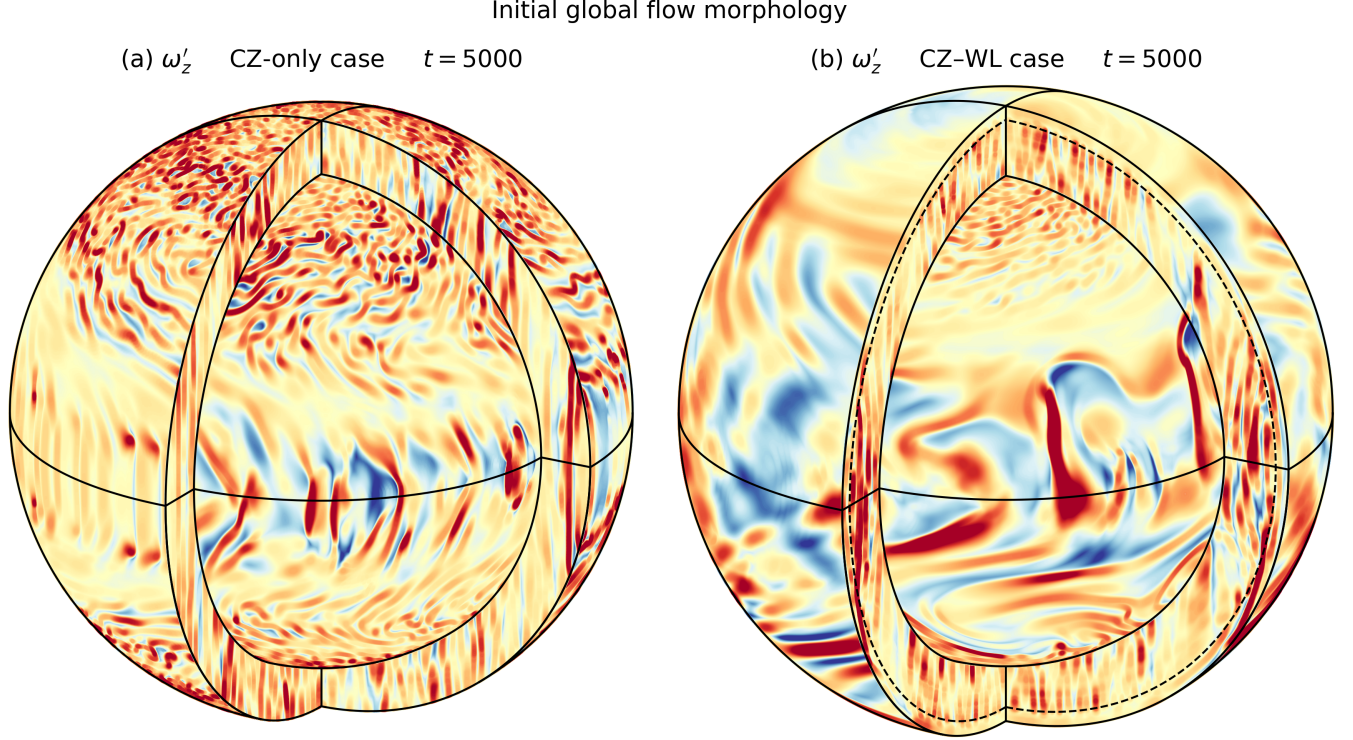


Figure 3. Spherical and meridional cutouts of our 3D shellular simulation domain, showing snapshots of the fluctuating axial vorticity ω'_z in (a) the CZ-only case and (b) the CZ-WL case. Each snapshot is taken near the beginning of the simulation when there are multiple jets ($t = 5000$). The inner and outer spherical surfaces bounding the cutout are taken just above and below the inner and outer domain boundaries, respectively. The meridional surfaces bounding the cutouts are located 90° apart, at $\phi = -30^\circ$ and $\phi = 60^\circ$, with $\phi = 0^\circ$ being the central viewing longitude (each cutout is viewed from the latitude $\theta = 20^\circ$). Each radial level is normalized separately by the rms of ω'_z at that level. In panel (b), the interface $r = r_c$ is marked by dashed black curves. The relative sizes of the plots reflect the larger domain size for the CZ-WL case. An animated version of this figure is available in the online journal. In the 30-second animation, the evolution of ω'_z for the two cases is shown side by side for an interval of length ≈ 720 (in simulation time units) centered about $t = 5000$. In each animation, time is measured from beginning of the animation. Animated versions of the separate panels are also available for download at <https://doi.org/10.5281/zenodo.20332552> and for viewing at <https://youtube.com/shorts/YSKIkOU8nYI> (CZ-only case), <https://youtube.com/shorts/hl5Ipgm9unU> (CZ-WL case), and https://youtu.be/9rYgFe9U_ag (both cases side-by-side).

various Reynolds numbers all exceeding 140. The flow amplitudes themselves are quite small, with dimensional values typically only a few percent of $2\Omega_0 H$.

Note that despite the prominent organization of the convective flow structures into axially aligned columns, the motion in each simulation's CZ is fully 3D. We emphasize this point in Figure 4, which shows the fluctuating flow amplitudes of each velocity vector component (both cylindrical and spherical) separately for both the CZ-only and CZ-WL cases. Except near the boundaries, all flow components have comparable amplitudes in the CZ. In particular, $|u'_z|$ is significant, which we would not expect for a thin stationary column of axial vorticity. This can be understood because the columns are *not* stationary. Instead, they are advected by neighboring columns and move in the λ direction, undergo-

ing significant stretching and compression because of the tilted spherical boundaries, and thus generating significant u'_z .

In the WL of the CZ-WL case, the radial velocity amplitude drops off significantly and becomes about 20 times weaker than the horizontal velocity components. This indicates that unlike the motion in the CZ, the motion in the WL *is* primarily 2D, being composed of pancake structures of vertical vorticity ω'_r .

3.2. Initial jets

Both types of eddies, Busse columns and pancake vortices, initially drive multiple jets, the structures of which are shown in Figure 5. The two cases are largely comparable: in the CZ-only case there are seven jets in the northern hemisphere and five jets in the southern hemisphere, whereas in the CZ-WL case, there are five

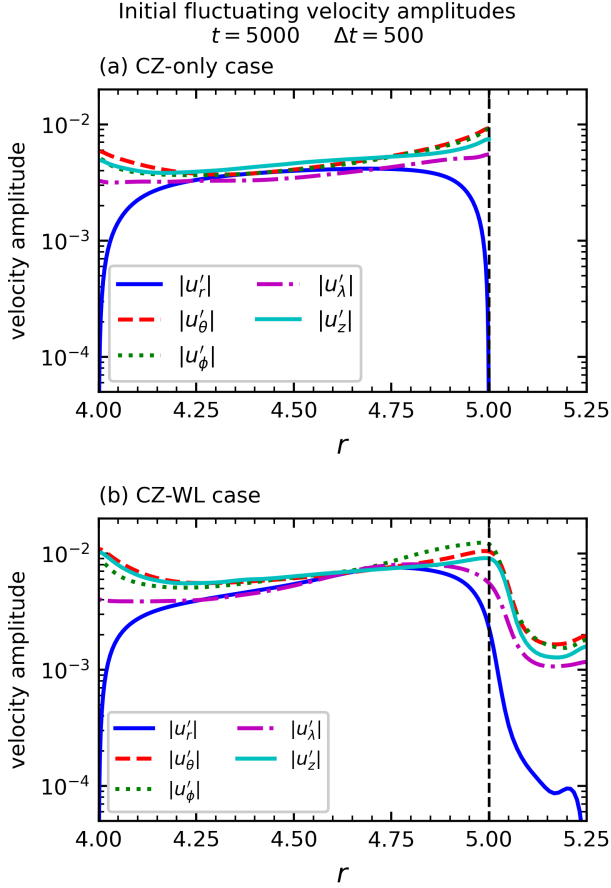


Figure 4. Fluctuating flow amplitudes for the various velocity components as functions of radius for (a) the CZ-only case and (b) the CZ–WL case, averaged in time over $t = 5000 \pm 250$. Here, the absolute values denote the rms of the enclosed quantity, with the mean taken over time and horizontal (i.e., spherical) surfaces. For example, $|u'_r| := \langle (u'_r)^2 \rangle_{\text{sph}, t}^{1/2}$.

jets in each hemisphere (the equatorial jet gets double-counted). In each case, there is one large superrotating jet just outside the tangent cylinder.

Despite this similarity in the overall structure of the jets, the jets in the CZ–WL case are of significantly higher amplitude and have less cylindrically aligned isocontours of zonal flow in the bulk of the CZ. Indeed, in the WL, particularly at low to mid latitudes, the isocontours are closer to radial alignment than cylindrical alignment. We now verify that this is due to a modification of the thermal wind balance by the presence of our idealized WL, which results in a large cell of meridional circulation in the WL which transports heat.

3.3. Initial meridional circulation

In addition to the mean zonal flow, there is also a mean meridional circulation, which is generally described by the vector mean mass flux $\langle \tilde{\rho} \mathbf{u}_m \rangle$, where

$$\mathbf{u}_m := u_r \hat{e}_r + u_\theta \hat{e}_\theta = u_\lambda \hat{e}_\lambda + u_z \hat{e}_z \quad (28)$$

represents the flow components in the meridional plane.

Because $\nabla \cdot \langle \tilde{\rho} \mathbf{u}_m \rangle \equiv 0$, we can define the meridional-flow streamfunction $\Psi(r, \theta, t)$, which satisfies $\langle \tilde{\rho} \mathbf{u}_m \rangle = \nabla \times [\Psi(\hat{e}_\phi / \lambda)]$, or

$$\langle \tilde{\rho} u_r \rangle = \frac{1}{r^2 \sin \theta} \frac{\partial \Psi}{\partial \theta} \quad \text{and} \quad \langle \tilde{\rho} u_\theta \rangle = -\frac{1}{r \sin \theta} \frac{\partial \Psi}{\partial r}. \quad (29)$$

The contours of Ψ then correspond to the streamlines of $\langle \mathbf{u}_m \rangle$ and the density of the contours corresponds to the magnitude of the mass flux $|\langle \tilde{\rho} \mathbf{u}_m \rangle|$. We choose the integration constant such that Ψ vanishes on the boundaries of the meridional plane, which must also be boundaries of circulation cells. Thus, the contours $\Psi \equiv 0$ correspond to the boundaries of the circulation cells and the sign of Ψ indicates the sense of circulation within a cell. Looking along positive ϕ (i.e., into the page), $\Psi > 0$ indicates clockwise circulation and $\Psi < 0$ indicates counterclockwise circulation.

Figure 6 shows the initial meridional circulation profiles for both cases. In the CZ, except near the boundaries, the circulation cells are largely aligned with the rotation axis and there are many alternating clockwise/counterclockwise cells, commensurate with the multiple jets. The two circulation profiles are largely similar in the CZ.

In the WL of the CZ–WL case, the meridional flow is quite different. It is aligned primarily along spherical rather than cylindrical surfaces. Although there is some imprinting of the CZ’s multiple circulation cells upward, the bulk of the WL is dominated by a single counterclockwise cell (occupying low to mid-latitudes) in the northern hemisphere and a clockwise cell in the southern hemisphere. These two cells are also the locations of the significant contour tilts of mean zonal flow in Figure 5(b). For each hemisphere, this monocellular flow allows significant transport of heat in latitude and resultant large-scale baroclinicity. We remark that the absence of substantial multicellular meridional circulation in the idealized WL is interesting in light of Juno observations, which indicate the presence of many circulation cells (Ferrel-like cells) in the Jovian WL (K. Duer et al. 2021).

3.4. Thermal Wind Balance of the Initial Jets

To elucidate why the contour tilts of mean zonal flow are so different in each case, we consider the mainte-

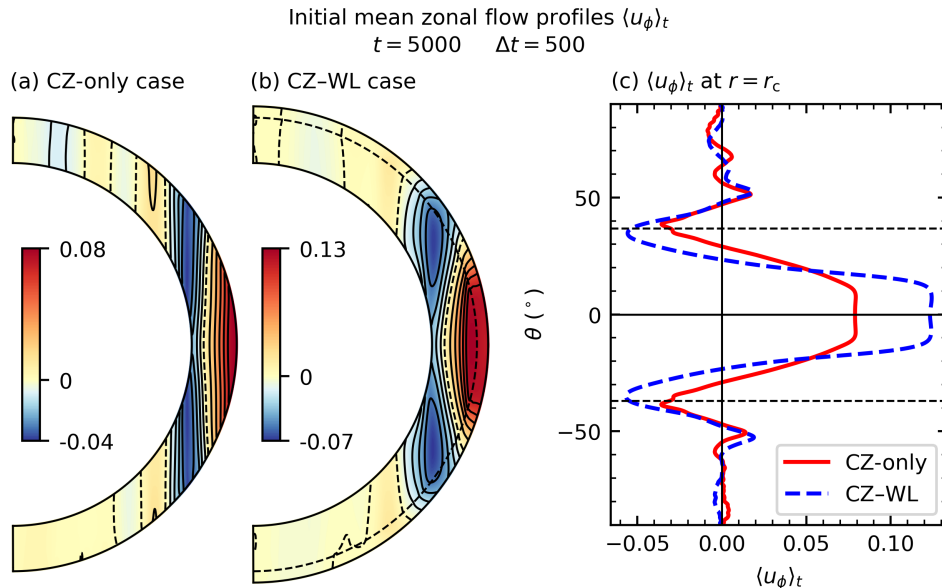


Figure 5. Temporally averaged mean zonal flow $\langle u_\phi \rangle_t$ in the meridional plane, showing the initial multiple jet structure in (a) the CZ-only case and (b) the CZ-WL case, averaged in time over the same interval $t = 5000 \pm 250$ as in Figure 4. Positive values are normalized separately from negative values and the nonzero contours (solid black curves) are equally spaced within each region of positive and negative values (the $\langle u_\phi \rangle_t \equiv 0$ contours are dashed). In panel (b), the CZ-WL boundary ($r = r_c$) is marked by the dashed semicircle. (c) Comparison of the latitudinal profiles of zonal flow at the top of the CZ ($r = r_c$) in the two cases. The horizontal dashed black lines denote the location of the tangent cylinder at $r = r_c$ ($\theta = 36.9^\circ$).

nance of the meridional flow. For high rotational constraint, this often takes the form of a special type of thermal wind balance appropriate for deep and shallow atmospheres alike (e.g., L. I. Matilsky 2023).⁵ Taking the mean zonal component of the curl of the momentum equation (17) and dropping the viscous and Reynolds-stress terms, we find

$$\frac{\partial \langle u_\phi \rangle_t^2}{\partial z} + \text{Ro}_c^2 \tilde{g} \sin \theta \frac{\partial \hat{s}}{\partial \theta} \approx 0. \quad (30)$$

which is the (nondimensional) canonical form thermal wind balance for deep atmospheres. The left-most term is called the centrifugal term because of its resemblance to a centrifugal force and the right-most term is the baroclinic term arising from latitudinal entropy gradients.

Figure 7 shows the thermal wind balance during $t = 5000 \pm 250$ for each case, i.e., the two terms in Equation 30 and their sum. Overall, the balance is fairly good in each case, with the relative residual between the two terms only about 20% in the bulk of the layer (close to the boundaries, thermal wind balance is broken because

Ekman layers result in a large contribution from the viscous term). In large portions of the CZ-WL case’s bulk, the relative residual is even smaller, on the order of only a few percent. Analysis at subsequent times (not shown) shows that the balance improves as the steady state is approached, with the residual approaching just a few percent everywhere in the bulk for both cases in the equilibrated state.

In the WL of the CZ-WL case, the large tilts in the zonal flow’s isocontours show up as an increased amplitude of the centrifugal term at low to mid-latitudes, which is in turn balanced by enhanced baroclinicity. Analysis of the heat transport equation (not shown) reveals an advective-diffusive balance in the mean entropy equation (18), showing that the large baroclinicity is caused by advective transport from the two cells of meridional circulation at low to mid latitudes in the WL (Figure 6b). In summary, even our idealized WL can significantly alter the dynamics of the zonal jets by leading to enhanced heat transport by meridional circulation and a sizable modification of the thermal wind balance.

4. FORMATION OF JETS IN THE CZ

Figure 3 shows that in both cases, the convection largely takes the form of columnar rolls aligned with the rotation axis. We find that these columnar struc-

⁵ The traditional form of thermal wind balance (e.g., G. K. Vallis 2017, p. 87) is only applicable to shallow and/or strongly stratified fluid layers, such as the Earth’s atmosphere and oceans, for which the vertical extent of the motion is much less than the horizontal extent.

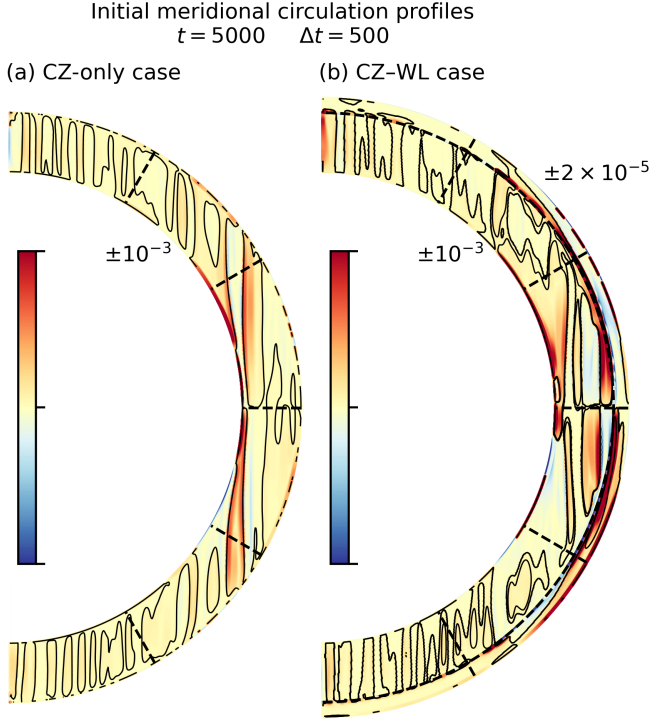


Figure 6. Meridional circulation profiles $|\langle \tilde{\rho} \mathbf{u}_m \rangle_t| \text{sgn}(\langle \Psi \rangle_t)$ (see Equations 28 and 29) for (a) the CZ-only case and (b) the CZ–WL case, plotted in the meridional plane and averaged over $t = 5000 \pm 250$. Red tones indicate clockwise circulation and blue tones indicate counterclockwise circulation. Contours of $\langle \Psi \rangle_t \equiv 0$ (the circulation cell boundaries) are also shown. In panel (b), the color table is saturated separately for the CZ (extreme values $\pm 10^{-3}$, also used for the CZ-only case) and the WL (extreme values $\pm 2 \times 10^{-5}$). This allows the rendering of the small-amplitude flow in the WL. The dashed semicircle denotes $r = r_c$.

tures share many properties explored by (e.g.) F. H. Busse (2002), which is why we refer to them as Busse columns. As discussed in Section 1.3, Busse columns can drive cylindrically aligned jets in a quasi-2D framework through the topographic β -effect. In this section, we thus consider the homogenization of $\langle Q_z \rangle_t$ (over the early time interval $t = 5000 \pm 250$), the formation of PV staircases, and the width of the jets relative to the topographic Rhines scale. In terms of the nondimensional variables, Equation (3) gives

$$Q_z = \frac{\omega_z + 1}{H} = \frac{\omega_z}{H} + f_{\text{topo}} > 0, \quad (31)$$

$$f_{\text{topo}} := \frac{1}{H}, \quad (32)$$

$$\text{and } \beta_{\text{topo}} := -H \frac{df_{\text{topo}}}{d\lambda} = \frac{1}{H} \frac{dH}{d\lambda}, \quad (33)$$

where, from Figure 1, we explicitly calculate

$$H(\lambda) := \begin{cases} 2\sqrt{r_c^2 - \lambda^2} & \lambda \geq r_{\text{in}} \\ 2(\sqrt{r_c^2 - \lambda^2} - \sqrt{r_{\text{in}}^2 - \lambda^2}), & \lambda < r_{\text{in}} \end{cases} \quad (34)$$

To avoid a discontinuity in H , we take H inside the tangent cylinder to be double the axial distance between the shells.

Figure 8 shows the mean PV $\langle Q_z \rangle_t$ associated with the initial jets.⁶ The PV contours are almost entirely cylindrically aligned in the CZ of each case, but tilt significantly in the WL of the CZ–WL case at low to mid latitudes, just like the contours of $\langle u_\phi \rangle_t$. This again suggests that Q_z is the right form for PV, but only in the CZ. In Figure 8(c), it is clear that there are some suggestions of staircase-like structures in PV outside the tangent cylinder, with regions of roughly homogeneous $\langle Q_z \rangle_t$ in between the high-latitude jets. As noted in Section 1.3, staircases in PV are thought to be one description of how multiple jets form in quasi-2D turbulence (e.g., G. K. Vallis 2017).

To increase the signal of the initial staircase structure in PV (and to respect the axial symmetry of the columns in the CZ), we plot the axially averaged flow profiles for mean zonal flow velocity (Figure 9) and PV (Figure 10). To capture the hemispheric asymmetry of the flow inside the tangent cylinder, we average in z over each hemisphere separately and plot the results as a function of the coordinate

$$\Lambda(\lambda, \theta) := (r_{\text{out}} - \lambda) \text{sgn}(\theta), \quad (35)$$

where $\text{sgn}()$ is the sign function. The coordinate Λ falls in the range $(-r_{\text{out}}, r_{\text{out}})$ and is positive in the northern hemisphere and negative in the southern hemisphere, with $\Lambda = 0$ marking the equator at the outer surface. Outside the tangent cylinder (the region $|\Lambda| \leq r_{\text{out}} - r_{\text{in}}$), we average over the full range of z , so all z -averaged functions of Λ are symmetric outside the tangent cylinder but asymmetric inside it.

In Figure 9, we locate the maxima and minima of the zonal flow $\langle u_\phi \rangle_{z,t}$ and mark these extrema with thin dotted lines in Figures 9–11. As is apparent from Figure 10, inside the tangent cylinder, PV is partially homogenized between each pair of extrema, which is what gives rise to the staircase structure in $\langle Q_z \rangle_{z,t}$ (Figure 8c). Because

⁶ Note that ideally $H(\lambda)$ would always represent the axial distance between the bounding spheres of the CZ, $r \equiv r_{\text{in}}$ and $r \equiv r_c$ (as in Figure 1). However, this would lead to undefined H and β_{topo} in the WL of the CZ–WL case. To simplify the calculations, in the CZ–WL case, we take H to be the axial distance between the bounding spheres of the full domain (including the WL).

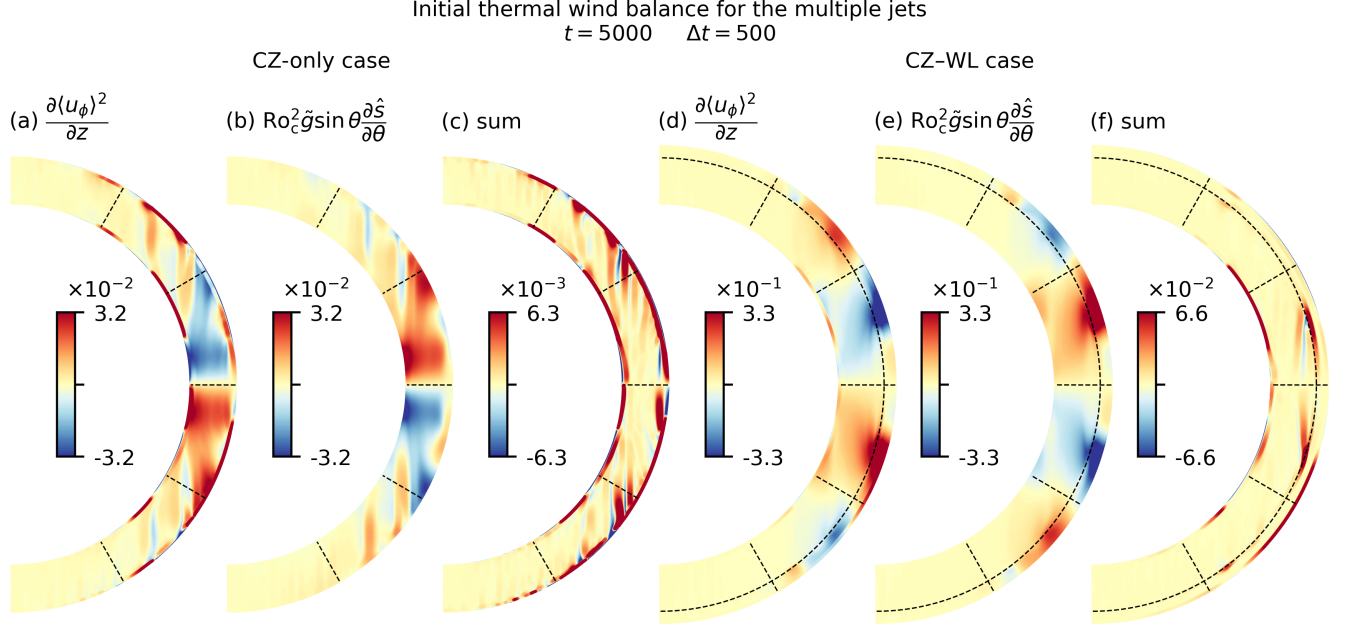


Figure 7. Thermal wind balance (Equation 30), averaged in time over $t = 5000 \pm 250$. The centrifugal term, baroclinic term, and their sum are plotted in the meridional plane for (a–c) the CZ-only case and (d–f) the CZ–WL case. As in other figures, the dashed semicircle in panel (b) denotes the CZ–WL interface.

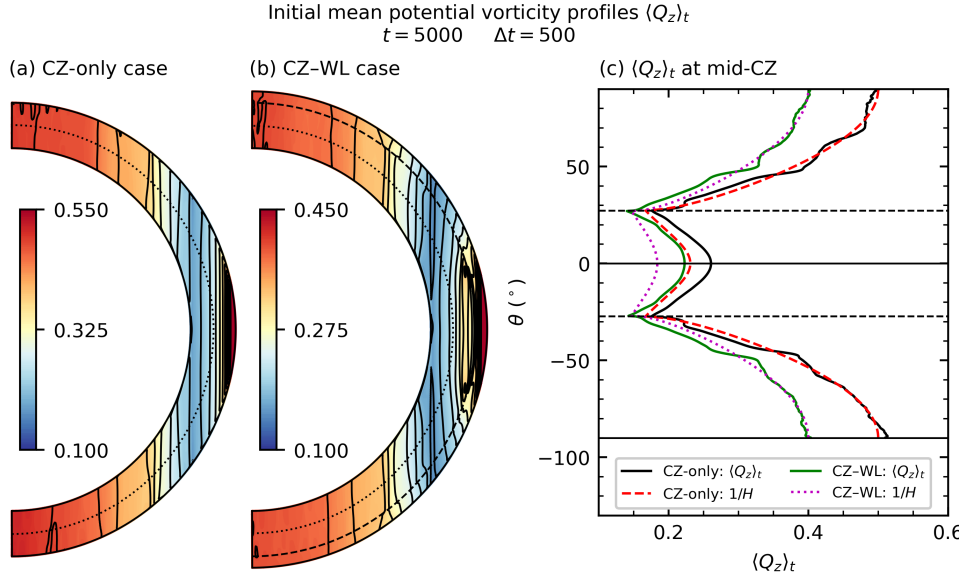


Figure 8. Temporally averaged mean potential vorticity $\langle Q_z \rangle_t$ in (a) the CZ-only case and (b) the CZ–WL case, averaged over the same interval $t = 5000 \pm 250$ as in Figures 4 and 5. All contours (solid black curves) are equally spaced. The radii $r = 4.5, 5$ are marked by the dotted and dashed semicircles, respectively. (c) Latitudinal profiles of $\langle Q_z \rangle_t$ and the planetary PV $f_{\text{topo}} = 1/H$ for both cases at mid-CZ ($r = 4.5$). The horizontal dashed black lines denote the location of the tangent cylinder at $r = 4.5$ ($\theta = 27.3^\circ$).

of the high level of turbulence and fully 3D character of the flow, the homogenization of PV between the jets is imperfect, but surprisingly good after the axial average.

Outside the tangent cylinder in the region of superrotation, the PV remains very close to the planetary PV

$f_{\text{topo}} = 1/H$. We believe that this is because the Busse columns are strongly constrained by the convex boundaries to transport angular momentum outward outside the tangent cylinder. If this outward angular momentum transport is the dominant effect, it interferes with

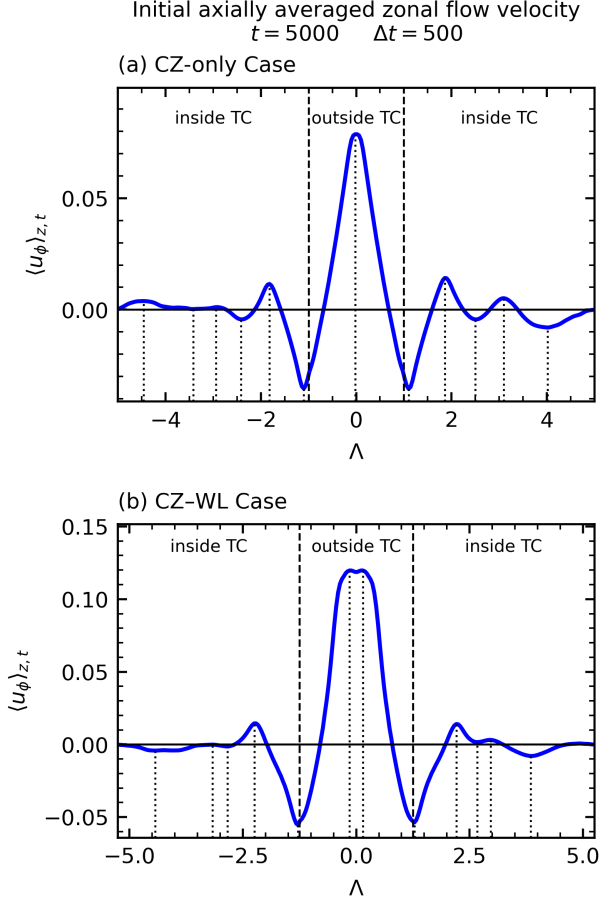


Figure 9. Temporally and axially averaged mean zonal flow velocity $\langle u_\phi \rangle_{z,t}$ in (a) the CZ-only case and (b) the CZ-WL case, averaged over the same interval $t = 5000 \pm 250$ as in Figures 4–8. The vertical dotted lines show the locations of the zonal flow’s maxima and minima and the dashed lines show the location of the tangent cylinder at $\Lambda = \pm(r_{\text{out}} - r_{\text{in}})$. Note that there are two minima at the tangent cylinder, obscuring the distinction between the lines there. All profiles are plotted with respect to the cylindrical coordinate Λ (see Equation 35). For clarity, the inside and outside of the tangent cylinder (TC) are labeled in this figure.

the full homogenization of PV. Note, however, that there is still partial homogenization of PV, with both profiles of $\langle Q_z \rangle_{z,t}$ slightly higher than f_{topo} . This is most obvious for the CZ-WL case, as evidenced by the raised “shoulders” in $\langle Q_z \rangle_{z,t}$ around $\Lambda = \pm 0.5$. We confirm these ideas explicitly in Section 6.

To estimate the topographic Rhines scale $L_{R,\text{topo}}$, we note that if Q_z is conserved ($D\omega_z/Dt \equiv 0$), then

$$\frac{D\omega_z}{Dt} - \beta_{\text{topo}} u_\lambda \approx 0, \quad (36)$$

where we have assumed low Rossby number ($|\omega_z| \ll 1$) to drop one of the nonlinear terms and we explicitly

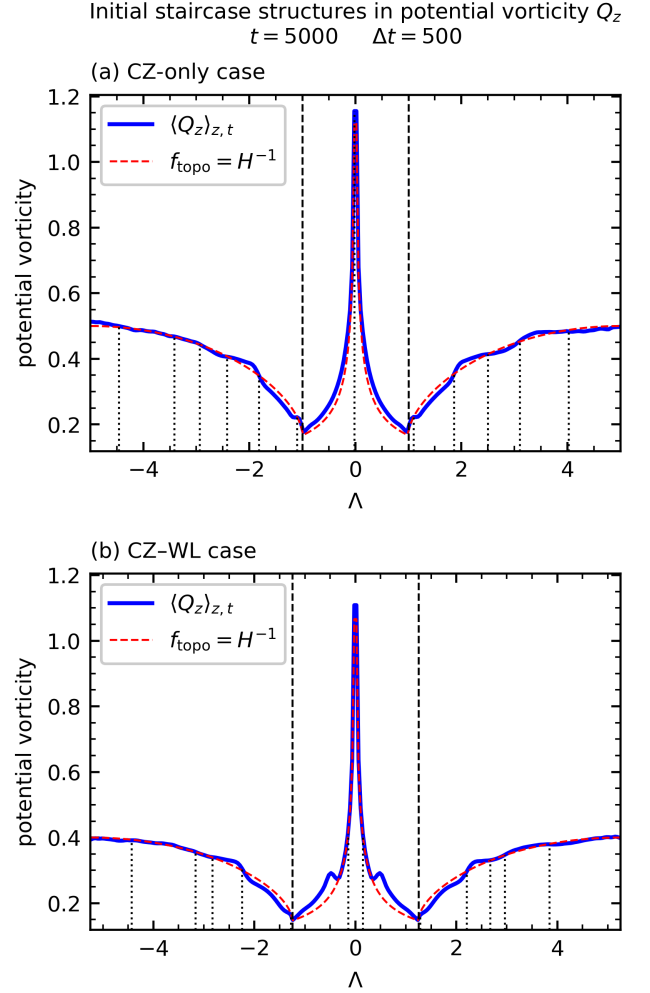


Figure 10. Temporally and axially averaged mean PV $\langle Q_z \rangle_{z,t}$ and the planetary PV $1/H$ in (a) the CZ-only case and (b) the CZ-WL case, averaged over $t = 5000 \pm 250$. The vertical dotted lines show the location the maxima and minima in the zonal flow profile $\langle u_\phi \rangle_{z,t}$ and the dashed lines show the location of the tangent cylinder.

compute

$$\beta_{\text{topo}}(\lambda) := \begin{cases} -\frac{\lambda}{r_c^2 - \lambda^2} & \lambda \geq r_{\text{in}} \\ \frac{\lambda}{\sqrt{r_c^2 - \lambda^2} \sqrt{r_{\text{in}}^2 - \lambda^2}} & \lambda < r_{\text{in}}. \end{cases} \quad (37)$$

Note that there is a sign change and discontinuity in β_{topo} at the tangent cylinder. There is also a singularity in β_{topo} as the tangent cylinder is approached from within, and another singularity at the equator. Physically, these singularities arise from locations where one of the bounding spheres becomes infinitely steep.

For eddies of a typical (nondimensional) length scale L and velocity amplitude U , we estimate $D\omega_z/Dt \sim$

U^2/L^2 and $\beta u_\theta \sim |\beta|U$. As expected, the nonlinear advection term dominates for small L . The Rhines scale (the crossover scale larger than which effects from the background PV gradient becomes important) is thus given by equating the magnitudes of the two terms in Equation (36), i.e., by setting

$$L = L_{R,\text{topo}}(\Lambda) := \sqrt{\frac{U(\Lambda)}{|\beta_{\text{topo}}|}}, \quad (38)$$

where $U(\Lambda)$ is the typical speed (at a given Λ) of the eddies under consideration. Eddies at different length scales will have different turnover speeds U and hence different topographic Rhines scales. In our simulations, however, U is typically dominated by the jet speed $\langle u_\phi \rangle$. Thus, to compute the Rhines scale of the jets themselves, we explicitly define

$$L_{R,\text{topo}}(\Lambda) := \sqrt{\frac{\langle |\mathbf{u}|^2 \rangle_{z,t}^{1/2}}{|\beta_{\text{topo}}|}}, \quad (39)$$

where we have replaced $U(\lambda)$ in Equation (38) with the typical speed of the total flow, including both turbulent and mean components. We now assess whether the Rhines scale defined in this way matches the actual local cylindrical width of the jets $L_{\text{jet},\lambda}(\Lambda)$ in each case's CZ. Considering the presence of the second spatial derivative of the mean flow in the term $D\langle \omega_z \rangle / Dt$, we define the latter cylindrical width as

$$L_{\text{jet},\lambda}(\Lambda) := \sqrt{\frac{\langle |\langle u_\phi \rangle_t| \rangle_z}{\langle |\partial^2 \langle u_\phi \rangle_t / \partial \lambda^2| \rangle_z}}. \quad (40)$$

Figure 11 shows the comparison between the local length scales $L_{R,\text{topo}}(\Lambda)$ and $L_{\text{jet}}(\Lambda)$. They match the best for the CZ–WL case, which also has slightly more convincing staircase-like structures in PV. Especially inside the tangent cylinder at high latitudes, the local jet width oscillates about the local Rhines scale as Λ varies in each case.

Overall, these results suggest that in the CZ region, quasi-homogenization of Q_z leads to multiple jets with a width comparable to an appropriately defined Rhines scale, as arguments from 2D fluid flow would suggest. However, there are significant departures from this simple picture owing to the fully 3D nature of the flow, with the biggest discrepancies occurring in the region of superrotation outside the tangent cylinder.

5. FORMATION OF JETS IN THE WL

In the WL, we have already seen that the flows consist of flattened pancake structures of radial vorticity, which

Initial Rhines scale versus jet length scale
(Deep driving: topographic β -effect and z-symmetry)
 $t = 5000 \quad \Delta t = 500$

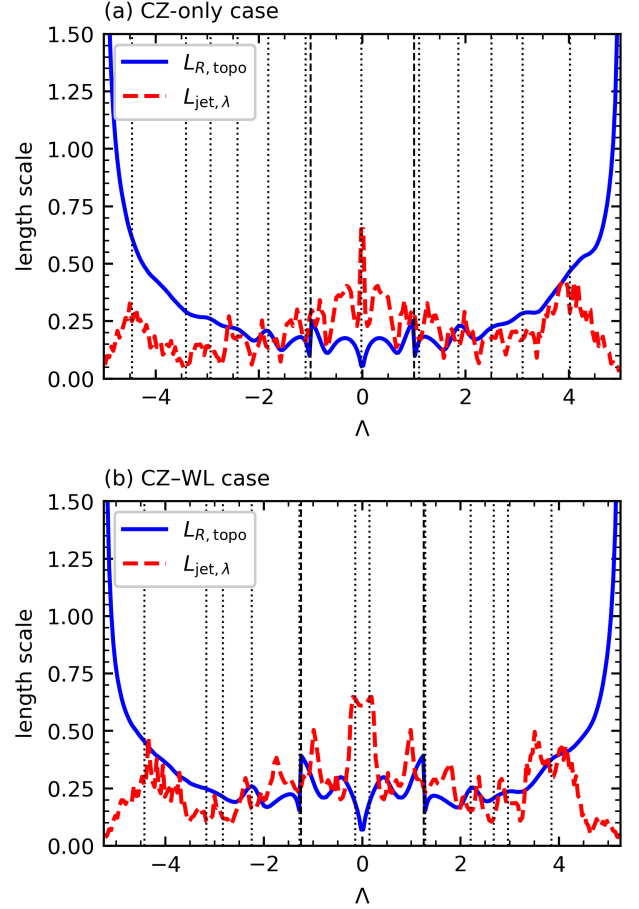


Figure 11. Rhines scale versus jet length scale (Equations 39 and 40), based on the temporally and axially averaged flows, in (a) the CZ-only case and (b) the CZ–WL case, averaged over $t = 5000 \pm 250$ and plotted as functions of Λ . The dotted lines show the locations of the maxima and minima in the zonal flow profile $\langle u_\phi \rangle_{z,t}$ and the dashed lines show the location of the tangent cylinder.

suggest from Section 1.3 that the appropriate form of PV is Q_r . By analogy with Section 4, the nondimensional form of Equation (2) leads to

$$Q_r := \omega_r + \sin \theta = \omega_r + f \quad (41)$$

$$f := \sin \theta, \quad (42)$$

$$\frac{D\omega_r}{Dt} + \beta u_\theta \approx 0, \quad (43)$$

$$\beta := \frac{df}{d\theta} = \frac{\cos \theta}{r_{\text{out}}}, \quad (44)$$

$$\text{and } L_R(\theta) := \sqrt{\frac{U(\theta)}{|\beta|}}, \quad (45)$$

where $U(\theta)$ is the typical speed (at a given θ) of the eddies under consideration and $L_R(\theta)$ is the locally varying (geometric) Rhines scale. In analogy with Section 4, we explicitly define the jet Rhines scale through

$$L_R(\theta) := \sqrt{\frac{\langle |\mathbf{u}|^2 \rangle_{r,t}^{1/2}}{\beta}} \quad (46)$$

and this should be comparable to the actual local latitudinal width of the jets in the WL,

$$L_{\text{jet},\theta}(\theta) := \sqrt{\frac{\langle |\langle u_\phi \rangle_t| \rangle_r r_{\text{out}}^2}{\langle |\partial^2 \langle u_\phi \rangle_t / \partial \theta^2| \rangle_z}}, \quad (47)$$

where we recall that $\langle \dots \rangle_r$ denotes a radial volume-weighted average over the WL.

Figure 12 shows the initial latitudinal structure of the WL's mean zonal flow $\langle u_\phi \rangle_{r,t}$, along with the initial staircases in $\langle Q_r \rangle_{r,t}$. It is clear from Figure 12(a) that the superrotating jet has a local minimum at the equator, meaning that the superrotation could be interpreted as being composed of three jets, as is the case on Jupiter. Furthermore, the staircase structure in $\langle Q_r \rangle_{r,t}$ is slightly more convincing than that of the CZ, with flatter steps in the staircase. However, very close to the equator ($|\theta| \leq 10^\circ$ or so), very little homogenization of PV occurs, and $\langle Q_r \rangle_{r,t}$ basically matches the planetary PV $f = \sin \theta$.

This suggests that the local length scales $L_R(\theta)$ and $L_{\text{jet},\theta}(\theta)$ should match slightly better than the CZ length scales $L_{R,\text{topo}}(\Lambda)$ and $L_{\text{jet},\lambda}(\Lambda)$ shown in Figure 11, at least away from the equator. This conclusion is borne out in Figure 13, which shows the comparison of $L_R(\theta)$ and $L_{\text{jet},\theta}(\theta)$ at $t = 5000 \pm 250$. The matching is very good at all latitudes except the very-near-equator region $|\theta| \leq 10^\circ$, i.e., the region of strongest superrotation. There, the jet width is a factor of several larger than the local Rhines scale would suggest. Figure 13, along with the fact that very little homogenization of PV seems to occur across the equator (Figure 12b), once again suggests the the superrotation in our simulations cannot be fully explained by quasi-2D arguments, even in the WL, where the motion basically *is* 2D (see Figure 4b).

We note that M. H. Heimpel et al. (2022) also performed an analysis of PV homogenization (for both Q_r and Q_z) for several models with a CZ underlying a stable layer similar to our CZ–WL case. In that work, Q_r and Q_z were plotted as functions of latitude for one radius in the CZ and one in the stable layer (see their Figs. 13 and 14). The staircase structures discussed in this work (see Figures 10 and 12) are qualitatively similar to those of M. H. Heimpel et al. (2022), however, the influence of our WL seems to be much stronger in our case due

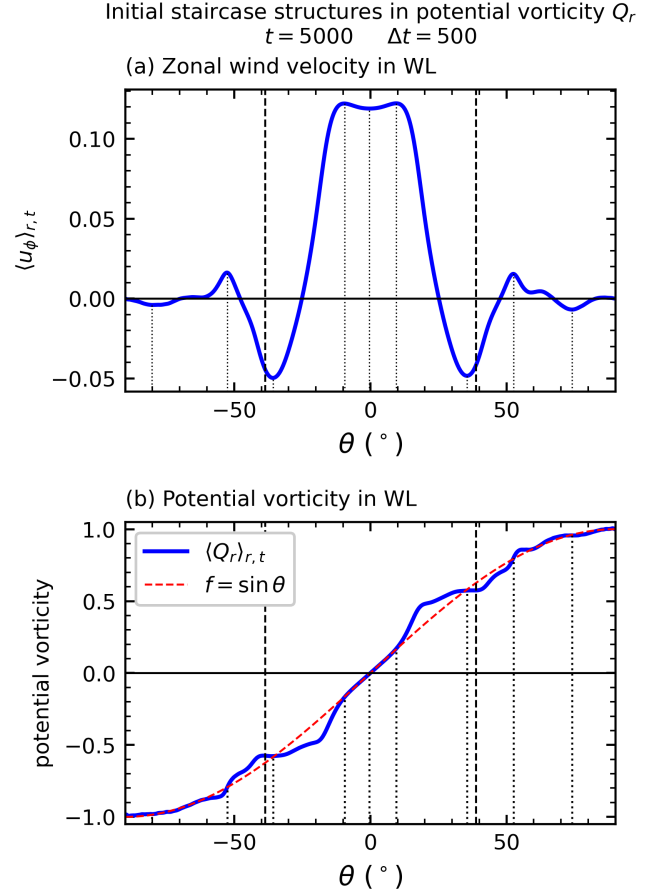


Figure 12. The CZ–WL case’s (a) mean zonal flow $\langle u_\phi \rangle_{r,t}$ and (b) mean PV $\langle Q_r \rangle_{r,t}$ (along with the planetary PV $\sin \theta$), both temporally averaged over the interval $t = 5000 \pm 250$. Recall that the radial average is always taken over the WL. The thin dotted lines show the location of the maxima and minima in the zonal flow profile $\langle u_\phi \rangle_{r,t}$ and the dashed lines show the location of tangent cylinder (here interpreted to be $|\theta| = \arccos(r_{\text{in}}/r_{\text{mwl}}) = 38.7^\circ$, where $r_{\text{mwl}} := (r_c + r_{\text{out}})/2$).

to its effects on thermal wind balance. This tilts the isocontours of $\langle u_\phi \rangle_t$ significantly more radially at low to mid latitudes in our WL and makes each layer have its distinct form of PV and appropriate averaging process: Q_z , averaged in z , as a function of Λ for the CZ and Q_r , averaged in r , as a function of θ for the WL.

6. SUPERROTATION

The presence of negative β_{topo} outside the tangent cylinder leads to an elegant argument for the generation of superrotation. Namely, for a jet of constant PV, $\langle Q_z \rangle = (\langle \omega_z \rangle + 1)/H = C > 0$ (where C is some positive constant) and hence $\partial \langle \omega_z \rangle / \partial \lambda = CdH/d\lambda$ or $\partial^2 \langle u_\phi \rangle / \partial \lambda^2 \approx CH\beta_{\text{topo}} < 0$. Hence, the single large

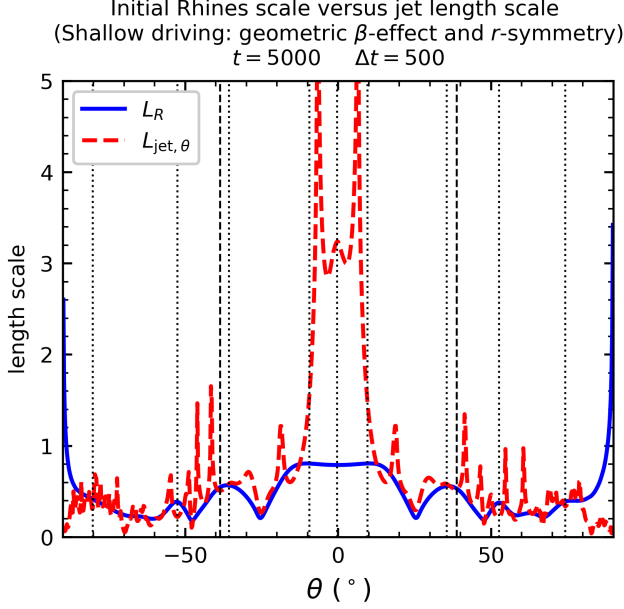


Figure 13. Rhines scale versus jet length scale (Equations 46 and 47), based on the temporally and radially averaged flows in the CZ–WL case’s WL, averaged over $t = 5000 \pm 250$. The thin dotted lines show the location of the maxima and minima in the zonal flow profile $\langle u_\phi \rangle_{r,t}$ and the dashed lines show the location of tangent cylinder $|\theta| = 38.7^\circ$.

jet outside the tangent cylinder is expected to have a local maximum in $\langle u_\phi \rangle$, i.e., be superrotating, if it has constant PV. However, the results of Sections 4 and 5 show that PV (either Q_z or Q_r) is rather far from constant in the region of superrotation. It thus appears that quasi-2D theory (namely the topographic β -effect) is insufficient to explain the form of superrotation achieved in our simulations.

Instead, superrotation may be studied by examining the transport of angular momentum, which is conserved in our models.⁷ Busse columns tend to transport angular momentum cylindrically outward and thus to low latitudes outside the tangent cylinder, causing equatorial superrotation. This is because the columns, in the presence of convex spherical-shell boundaries, typically have cross section which are flared outward, leading to a λ -varying tilt in the prograde direction—a result long expected from quasi-nonlinear stability analysis (e.g.,

⁷ In the continuous equations, total angular momentum would be conserved exactly, because the boundaries are impenetrable and stress-free. In our discrete implementation, we do not enforce strict conservation as a boundary condition. Nevertheless, total angular momentum remains conserved to about 1 in 10^6 in the CZ-only case and 1 in 10^4 in the CZ–WL case over the full run of each simulation.

F. H. Busse 2002). Figure 14 shows an example of this flaring pattern for our two simulations. The pattern is obvious, despite the strong nonlinearity of our simulations. Because of the prograde cross-section tilts, the fluctuating cylindrical velocity u'_λ is correlated with the fluctuating zonal velocity u'_ϕ such that $\langle u'_\lambda u'_\phi \rangle > 0$. Because of the flare, this means there is a cylindrically outward transport of angular momentum that is strongest close to the boundaries, resulting in a positive Reynolds-stress torque near the equator and a negative one near the tangent cylinder. This natural driver of equatorial superrotation, from the perspective of the quasi-linear stability analysis, is fundamentally linked to the presence of flare in the columns’ cross sections, which arises from convex spherical boundaries.

Note that both mechanisms for generating superrotation (the homogenization of PV Q_z and the flaring of Busse columns discussed further below) arise from the tilt of the bounding spherical surfaces. However, in the mechanism of PV homogenization, only the sign of the tilt ($dH/d\lambda < 0$) matters for superrotation, whereas for the flaring of Busse columns, the curvature of the boundaries ($d^2H/d\lambda^2$) is the reason for superrotation. The two mechanisms are thus related but may be distinct.

To quantify how Busse columns transport angular momentum in our simulations, as well as determine how the jets imprint into the WL, we analyze the full torque equation explicitly. The specific angular momentum density of the fluid is

$$\mathcal{L} := \lambda \left(\frac{\lambda}{2} + \langle u_\phi \rangle \right) = \lambda^2 \Omega, \quad (48)$$

where

$$\Omega := \frac{1}{2} + \frac{\langle u_\phi \rangle}{\lambda} \quad (49)$$

is the mean rotation rate of the fluid.

Multiplying the ϕ -component of the zonal mean of Equation (17) by λ yields the evolution equation for \mathcal{L} (or equivalently, for $\langle u_\phi \rangle$ or Ω):

$$\begin{aligned} \tilde{\rho} \frac{\partial \mathcal{L}}{\partial t} &= \tilde{\rho} \lambda \frac{\partial \langle u_\phi \rangle}{\partial t} = \tilde{\rho} \lambda^2 \frac{\partial \Omega}{\partial t} \\ &= -\nabla \cdot [\tilde{\rho} (\lambda \langle u'_\phi \mathbf{u}'_m \rangle) + \mathcal{L} \langle \mathbf{u}_m \rangle - \text{Ek} \tilde{\nu} \lambda^2 \nabla \Omega] \end{aligned} \quad (50a)$$

$$= \tau_{rs} + \tau_{mc} + \tau_v = \tau_{\text{tot}}, \quad (50b)$$

where we have defined the appropriate time-dependent torque densities:

$$\begin{aligned} \tau_{rs} &:= -\nabla \cdot (\tilde{\rho} (\lambda \langle u'_\phi \mathbf{u}'_m \rangle)) \\ &\quad (\text{Reynolds-stress torque}), \end{aligned} \quad (51a)$$

$$\tau_{mc} := -\langle \tilde{\rho} \mathbf{u}_m \rangle \cdot \nabla \mathcal{L}$$

(meridional-circulation torque), (51b)

$$\tau_v := \text{Ek} \nabla \cdot (\tilde{\rho} \tilde{\nu} \lambda^2 \nabla \Omega)$$

(viscous torque), (51c)

and $\tau_{\text{tot}} := \tau_{\text{rs}} + \tau_{\text{mc}} + \tau_v$

(total torque). (51d)

Figure 15 shows $\langle \tilde{\rho} \lambda u_\phi \rangle_t$ in the meridional plane, along with the three torques and their sum, for both cases over $t = 5000 \pm 250$. In the CZs of both cases, outside the tangent cylinder, the Reynolds-stress torque τ_{rs} is clearly responsible for driving the superrotation, being negative in a columnar pattern close to the edge of the tangent cylinder and positive in the equatorial regions further away. The other two torques (from viscosity and meridional circulation) tend to oppose the production of superrotation. At higher latitudes inside the tangent cylinder, there is a complicated three-way balance between the torques that leads to a banded pattern for the total torque τ_{tot} , which is offset slightly cylindrically inward from the actual jet structure exhibited by $\langle \tilde{\rho} \lambda u_\phi \rangle_t$. It is this offset, whose origins are not obvious, which is responsible for driving the high-latitude jets poleward with time, causing them to eventually disappear, as discussed in the following section.

In the WL of the CZ–WL case at low latitudes, the Reynolds-stress torque is extremely weak due to the small radial velocity. Instead, superrotation is driven here by both the viscous torque τ_v (at very low latitudes) and the meridional-circulation torque τ_{mc} (at mid-latitudes). This type of dual imprinting by the viscosity and circulation (especially for σ near unity) is expected from prior analyses of coupled convecting layer/stable layer systems in the solar context, for which the CZ’s meridional circulation and viscous stresses tend to “burrow” into the stable layer, despite being inhibited by the background stable stratification, carrying angular momentum with them (A. Clark 1973; E. A. Spiegel & J.-P. Zahn 1992; L. I. Matilsky et al. 2025, 2026). It shows that the WL’s superrotation is not driven primarily by nonlinear effects (either homogenization of PV or Reynolds stresses from Busse columns) but instead is the result of linear imprinting of the CZ’s superrotation upward. At higher latitudes, by contrast, the effects of the Reynolds stresses are stronger and multiple jets form mostly according to the quasi-2D ideas outlined in Section 5, namely the homogenization of Q_r on the scale L_R and subsequent formation of staircase structures.

7. JET MERGER AND MIGRATION

Up to this point, we have only analyzed the simulations for the relatively early time interval $t = 5000 \pm 250$ (see Figure 2). However, examining the full simula-

tions, we find that the high-latitude jets migrate poleward and/or merge on a very long timescale (but the superrotation outside the tangent cylinder remains basically steady). The end state for both simulations is a banded “fast-slow-fast” structure, consisting of three jets per hemisphere: the fast superrotating jet outside the tangent cylinder, and one pair of alternating slow and fast jets per hemisphere inside the tangent cylinder. This same fast-slow-fast structure of the zonal flow is often encountered for low-Rossby-number simulations in the solar context as well, where it is referred to as “Jupiter-like” (e.g., A. S. Brun et al. 2017).

Figure 16 shows the slow evolution of the jet structure in a time-latitude plot for the instantaneous mean zonal flow $\langle u_\phi \rangle$ at $r = r_c$ and as a sequence of profiles of the temporally averaged zonal flow $\langle u_\phi \rangle_t$ in the meridional plane. Interestingly, the superrotating jet outside the tangent cylinder does not significantly evolve and equilibrates relatively rapidly, after $O(1)$ diffusion time. The initially multiple high-latitude jets, however, slowly widen, migrate poleward, and/or merge, in a hemispherically asymmetric fashion, over $O(10)$ diffusion timescales, ultimately leaving only two high-latitude jets per hemisphere in the equilibrated state.

Overall, these results on jet migration in our simulations are similar to the work of S.-i. Takehiro et al. (2024), who found that the mid- and high-latitude jets in long-time integrations of a rapidly rotating Boussinesq fluid eventually merged/migrated and disappeared, leaving a still-evolving final state similar to the fast-slow-fast banded structure we find as well. Those models were significantly more rotationally constrained than our cases and had a thinner shell (in that work, $\text{Ek} = 1.5 \times 10^{-6}$, $\text{Ro}_c = 0.11$, and $\beta = 0.9$ compared to our $\text{Ek} = 5 \times 10^{-5}$, $\text{Ro}_c = 0.2$, and $\beta = 0.8$) and also utilized various hyperdiffusive parameterizations (whereas we have exclusively considered explicit Laplacian diffusivities). Here, we have thus affirmed the core result suggested by S.-i. Takehiro et al. (2024), that the final asymptotic steady state of global, 3D Jovian jet simulations may contain very few high-latitude jets. We do so for the actual asymptotic state and operate in the slightly different context of anelastic, more slowly rotating simulations, one of which includes a WL. We also suggest that the superrotating jet outside the tangent cylinder may be *part* of the asymptotic state and does not undergo significant evolution.

The true cause of jet migration/merging in the simulations is not well understood. Comparing Figures 15(a,e) (or equivalently, Figures 15(f,j)) we see that the total torque inside the tangent cylinder at early times has the same sign structure as the angular momentum associ-

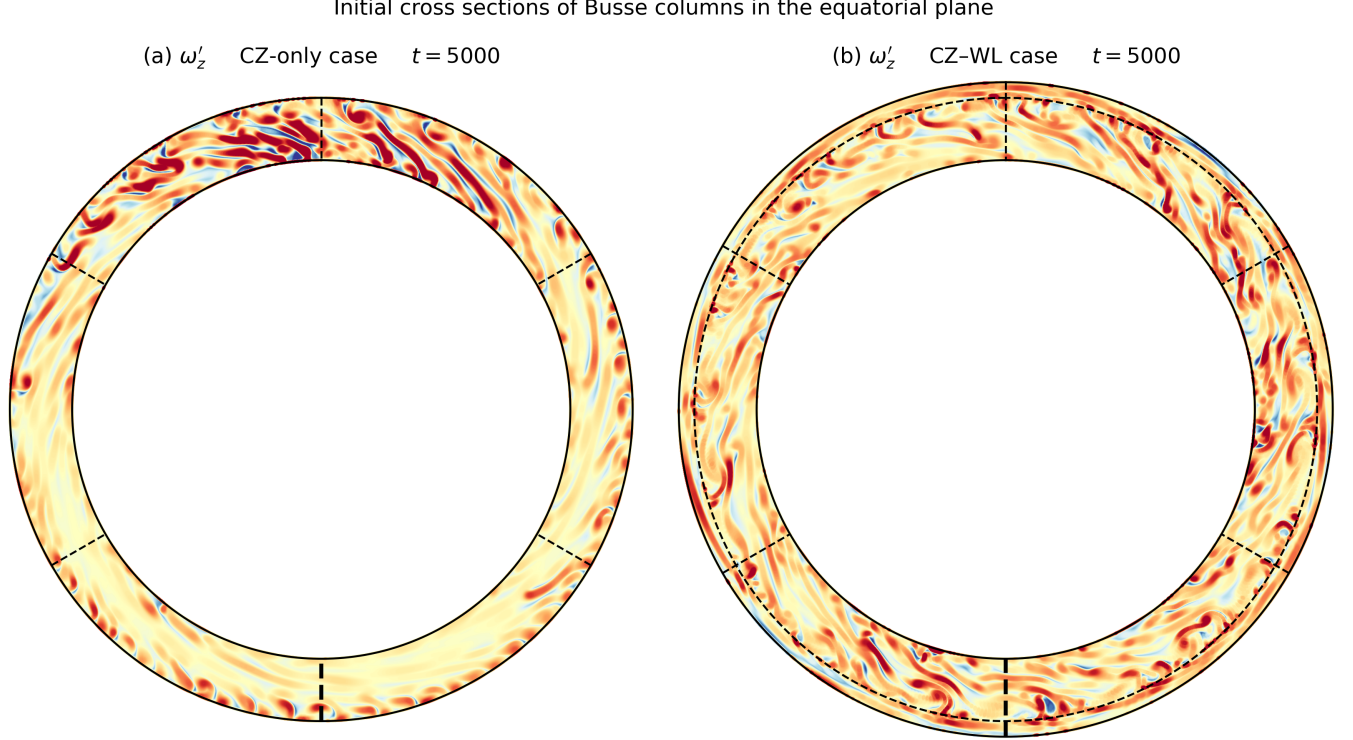


Figure 14. Cross sections of the Busse columns (columns of ω'_z) in the equatorial plane for (a) the CZ-only case and (b) the CZ-WL case at $t = 5000$ (the view is from the north pole). Red tones indicate cyclonic vorticity and blue tones indicate anticyclonic vorticity. The outward spirals of the columns in the CZ is obvious, while in the WL of the CZ-WL case, the columns have much larger horizontal extent and have no clear spiraling tendency. Just as in Figure 3, the fields are normalized separately at each radial level by the rms of ω'_z .

ated with the multiple jets, but is shifted slightly inward from the jets. This may at least suggest jet migration (as opposed to jet widening/merging), although similar analyses of the torque balance at later times (not shown) complicates this picture. In any event, it is far from obvious how (or why) the complicated three-way balance of torques at high latitudes serendipitously gives rise to a banded sign structure clearly correlated with, but displaced from, the jets. In a simpler model, [V. Morin & E. Dormy \(2006\)](#) found that steady multiple jets arose only in the presence of an Ekman drag, which halted the inverse cascade of energy to large scales. The lack of any such drag in our simulations thus may be affecting the stability of the jets.

Because of our current lack of clarity regarding jet migration, we postpone a detailed analysis to future work. We only note that the same quasi-2D arguments for high-latitude jet production, involving staircase-like structures of PV and associated Rhines scales, which were explored for $t = 5000 \pm 250$, appear to remain valid at subsequent times and in the equilibrated state. Figure 17 shows the evolution of the global jet width and Rhines scale for high latitudes as the jets migrate

and/or merge, as well as successive latitudinal profiles of the local jet widths and Rhines scales at different times (each like a transposed Figure 11).

Because the local Rhines scale, in both the CZ and WL, substantially underestimates the actual jet width in the region of superrotation, we exclude this region in the definition of the global length scales. Namely, we define the high-latitude globally averaged (time-dependent) topographic Rhines scale by

$$L_{R,\text{topo}}(t) = \left\langle \sqrt{\frac{\langle |\mathbf{u}|^2 \rangle^{1/2}}{|\beta_{\text{topo}}|}} \right\rangle_{\mathbf{v}}, \quad (52)$$

where the volume-average here is over the high-latitude CZ ($|\theta| > 45^\circ$, $r_{\text{in}} < r < r_c$). Similarly, we define the globally averaged high-latitude CZ jet width by

$$L_{\text{jet},\lambda}(t) = \left\langle \sqrt{\frac{|\langle u_\phi \rangle|}{|\partial^2 \langle u_\phi \rangle / \partial \lambda^2|}} \right\rangle_{\mathbf{v}}. \quad (53)$$

From Figure 17, it is clear that the high-latitude length scales match fairly well at all times and both exhibit slow monotonic growth with time. (Note that

Initial torque balance for the multiple jets
 $t = 5000 \quad \Delta t = 500$

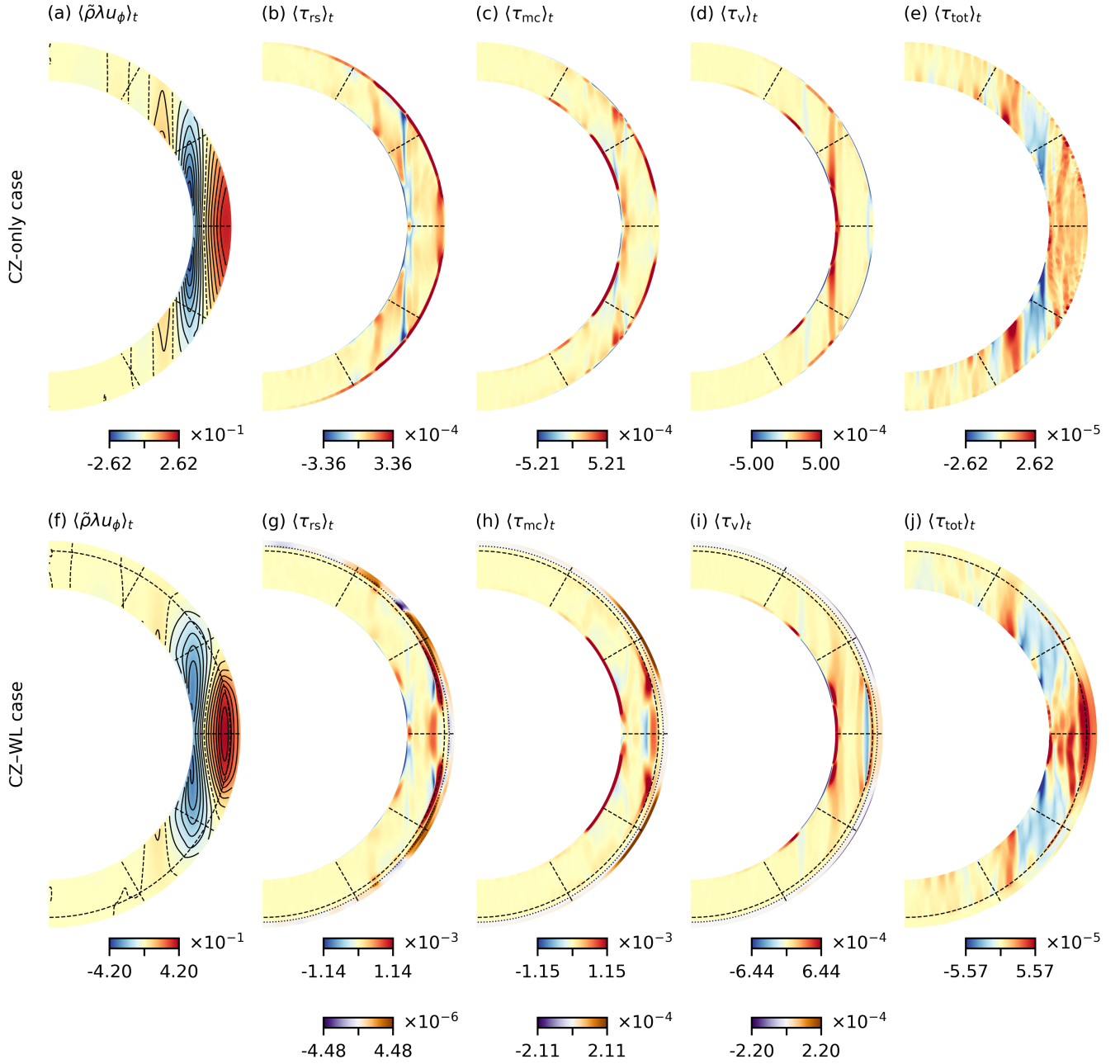


Figure 15. All terms in the torque equation (see Equations 50 and 51) in the meridional plane, zonally and temporally averaged (over $t = 5000 \pm 250$) for (a–e) the CZ-only case and (f–j) the CZ-WL case. Red tones denote positive values for the torque (i.e., tending to produce prograde zonal flow in the rotating frame) and blue tones denote negative values (tending to produce retrograde zonal flow). In the plots of $\bar{\rho} \lambda \langle u_\phi \rangle_t$ (left-most column), the contours are equally spaced and the zero contour is dashed. In the bottom row, the dashed semicircles denote $r = r_c$. In the plots for $\langle \tau_{rs} \rangle_t$, $\langle \tau_{mc} \rangle_t$, and $\langle \tau_v \rangle_t$ (middle three columns) a separate color table (purple/orange) is used for the upper WL ($r_{mwl} < r < r_{out}$) and the dotted semicircles mark $r = r_{mwl}$, where $r_{mwl} := (r_c + r_{out})/2$.

if the low latitudes—the superrotation—are included in the definitions 52 and 53, the jet length scale $L_{jet,\lambda}(t)$ is systematically about twice as large as the Rhines scale

$L_{R,\lambda}(t)$ at all times.) Furthermore, at any given time, the local length scales match reasonably well, except in the region of superrotation outside the tangent cylinder,

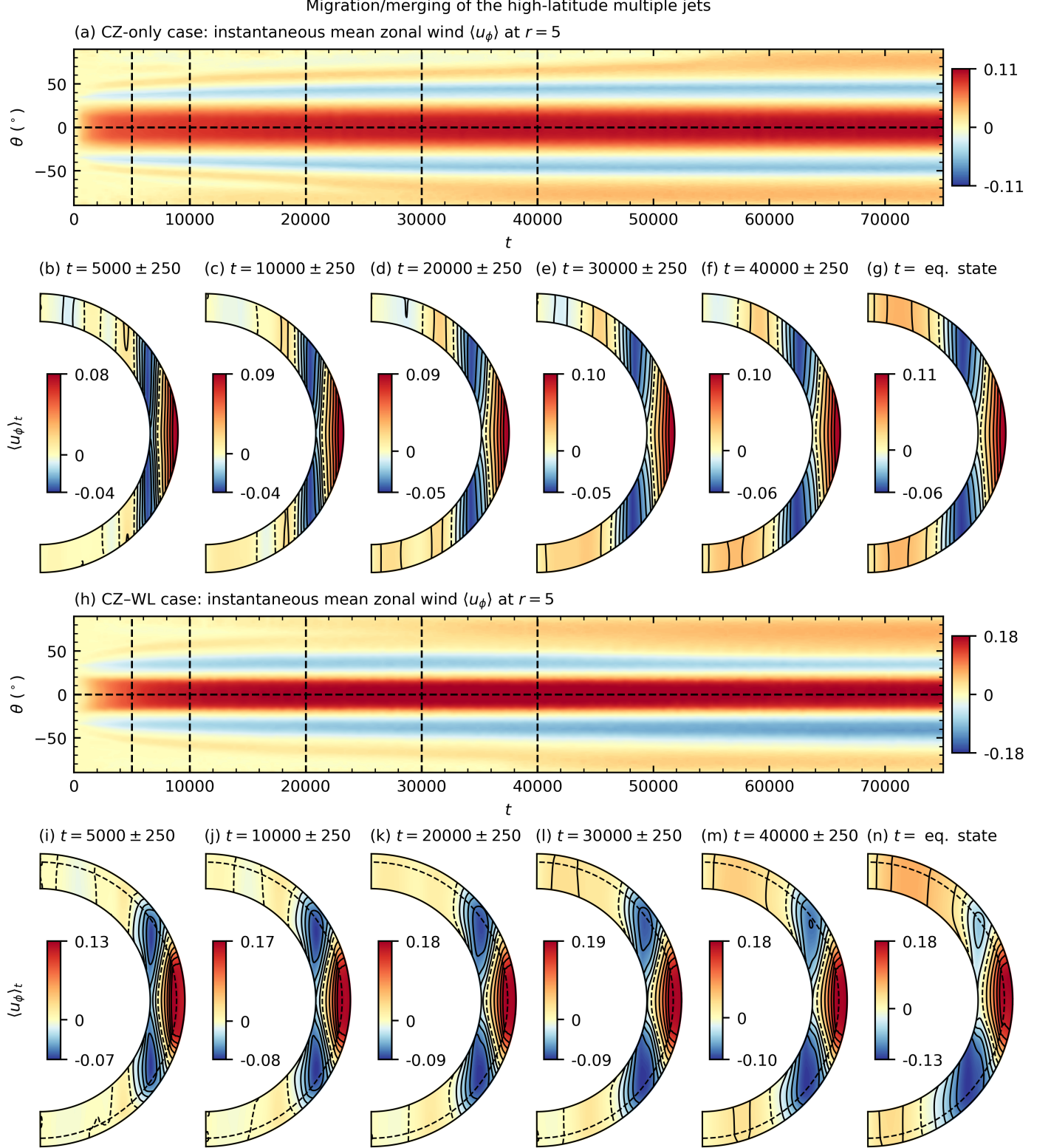


Figure 16. (a) Mean zonal flow velocity $\langle u_\phi \rangle$ at $r = r_c$ for the CZ-only case, plotted as a function of time and latitude. (b–f) Sequence of mean zonal flow profiles $\langle u_\phi \rangle_t$, averaged over the indicated time-intervals, as the high-latitude jets migrate poleward. In (b–e), the center of the indicated time intervals correspond to the vertical dashed lines in (a). In (g), the interval corresponds to the equilibrated state, which is roughly $t = (100000, 384000)$ for the CZ-only case. The contours are equally spaced separately for the positive and negative regions of the (binormalized) color table and the zero contour is dashed. (h–n) The same as (a–g), but for the CZ–WL case. In (i–n) the interface $r = r_c$ is shown as the dashed semicircle. In (b–g), the panels have been shrunk slightly to show the relative sizes of the two simulation domains. In (n), the equilibrated state for the CZ–WL case is roughly $t = (150000, 235000)$. Note that in our chosen units, the diffusion timescales are $\text{Ek}^{-1} = 22400$ (viscous) and $\text{Pr}/\text{Ek} = 11200$ (thermal).

and grow locally in concert with one another. In fact, the comparison between $L_{R,\text{topo}}(\Lambda)$ and $L_{\text{jet},\lambda}(\Lambda)$ generally improves as time progresses. We suppose that this is because the global high-latitude Rhines scale initially increases more rapidly than the jet width.

Overall, we interpret Figure 17 as follows. The initial crossover scale $L_{R,\text{topo}}(t)$ for the high-latitude jets is achieved early on (say around $t = 1000$) in both simulations. This funnels energy from the turbulent convection into the large-scale zonal flow in the manner of G. K. Vallis & M. E. Maltrud (1993). The jets then slowly build up enough energy (after about $t = 20000$, or ~ 2 thermal diffusion times) for their widths to catch up to the Rhines scale. Both length scales then continue to grow with time as the jets receive more and more energy from the turbulent cascade. The process only stops once the final equilibrium (set by a complicated three-way balance of torques, as well as thermal wind balance and equilibration of the heat equation) is achieved. Apparently for our simulations, and those of S.-i. Takehiro et al. 2024 at least, there is no process in the equilibrated state to dissipate the energy of the jets at sufficiently low energy levels for the eddy speeds (and hence the Rhines scales) to remain small. The jet width thus cannot remain small enough to sustain multiple high-latitude jets in the domain.

The absence of a dissipation mechanism for the inverse cascade at large scales greater than the crossover scale is well known. For example, G. K. Vallis & M. E. Maltrud (1993) found that the β -effect only redirects the inverse energy cascade into the zonal flows, but it does not actually stop the cascade at the crossover scale. A scale-independent linear drag to rigid rotation, say of the form $-r_d u_\phi$, on the right-hand side of the specific zonal momentum equation (where r_d has the dimensions of inverse time) has been implemented in 2D models in order to sustain steady high-latitude jets (e.g., G. P. Williams 1978; G. K. Vallis & M. E. Maltrud 1993; G. P. Williams 2002; Y. Lian & A. P. Showman 2008; Y. Zeng et al. 2025). The absence of any such drag in 3D models like ours and those of S.-i. Takehiro et al. (2024) thus may be responsible for the ultimate disappearance of multiple high-latitude jets. However, because of the intricacy and extreme slowness of the equilibration, at least in the simulations presented here, it is far from clear whether implementing a linear drag (and for what value of r_d) would solve the problem of disappearing jets in 3D, nor is the physical origin of such a drag obvious in a gaseous planet.

8. DISCUSSION

We have implemented two global, 3D anelastic simulations of the fluid equations in rapidly rotating spherical shells in order to assess the influence of an idealized “WL” (in this case, simply a stably stratified layer) atop a CZ, as well as to verify whether quasi-2D arguments involving PV homogenization/Reynolds stresses from Rossby waves could explain the formation of multiple jets and superrotation. In both simulations, a CZ-only case and a CZ-WL case, we found that multiple jets form at early times, with one large superrotating jet outside the tangent cylinder. At high latitudes inside the tangent cylinder, we verified that the quasi-2D arguments work rather well and multiple jets form with a locally and temporally varying Rhines scale ($L_{R,\text{topo}}$ or L_R ; see Equations 39, 46, and 52). In the CZ, the relevant PV is $Q_z = (\omega_z + 1)/H$ (see Equation 31) and the Rhines scale $L_{R,\text{topo}}$ is affected by the profile $\beta_{\text{topo}} = H^{-1}dH/d\lambda$ associated with the topographic β -effect (see Equation 37). In the WL by contrast, the relevant PV is $Q_r = \omega_r + \sin\theta$ and the Rhines scale L_R is affected by the familiar profile of $\beta = \cos\theta/r_{\text{out}}$ associated with the geometric β -effect (see Equations 41 and 44).

Outside the tangent cylinder, the superrotating jet appears to be driven primarily by the Reynolds stresses associated with flared Busse columns in the CZ (see Figures 14 and 15), where the flare is a result of the convex spherical boundaries. Nonetheless, the profiles of $\langle Q_z \rangle_{z,t}$ shown in Figure 10 suggest that some homogenization of Q_z occurs even outside the tangent cylinder. In the WL of the CZ-WL case, the superrotation is imprinted upward from the CZ by a combination of burrowing meridional circulation and viscosity, with negligible contribution from the Reynolds stresses (or equivalently, negligible homogenization of Q_r).

Apart from altering the form of conserved PV, the WL serves to significantly tilt the isocontours of the zonal flow away from alignment with the rotation axis. We have verified that this occurs due to the monocellular structure of the meridional circulation in the each hemisphere of the WL, leading to an increase in baroclinicity and subsequent adjustment of the thermal wind, as shown in Figures 6 and 7.

Finally, we found that in both cases, the system evolves very slowly at high latitudes to finally reach equilibration after $O(10)$ diffusion times, whereas the low-latitude superrotation equilibrates fairly rapidly, after $O(1)$ diffusion time. During high-latitude equilibration, the multiple high-latitude jets slowly migrate and/or merge. Their monotonically increasing width at any given instant is determined by the instantaneous

Evolution of high-latitude topographic Rhines scale $L_{R, \text{topo}}(t)$ during jet migration

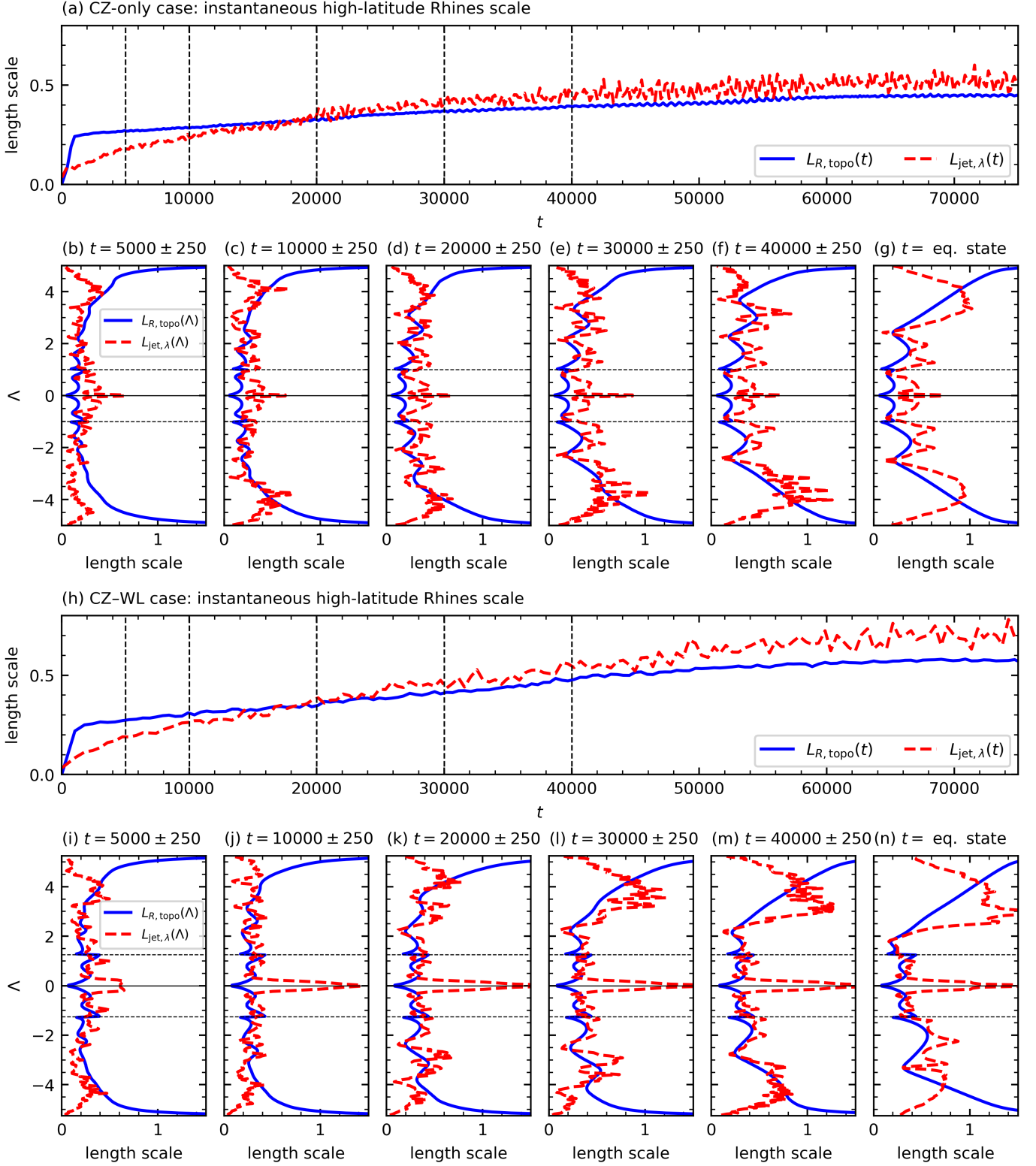


Figure 17. (a) Comparison of the time-dependent high-latitude length scales $L_{R, \lambda}(t)$ and $L_{\text{jet}, \lambda}(t)$ for the CZ-only case (see Equations 52 and 53). (b–f) Sequence of comparisons between the local CZ length scales $L_{R, \lambda}(\Lambda)$ and $L_{\text{jet}, \lambda}(\Lambda)$, averaged over the indicated time-intervals (see Equations 39 and 40). The horizontal solid line denotes $\Lambda = 0$ and the dashed lines denote the edge of the tangent cylinder at $\Lambda = \pm(r_{\text{out}} - r_{\text{in}})$. In (b–e), the center of the indicated time intervals correspond to the vertical dashed lines in (a). In (g), the interval corresponds to the equilibrated state (h–n). The same as (a–g), but for the CZ-WL case.

high-latitude Rhines scale (Equation 52), which also increases with time (see Figure 17).

To summarize, we address the questions laid out in Section 1 as follows:

1. The final steady state of zonal flow in our simulations consists of a “fast-slow-fast” pattern with very few high-latitude jets, similar to S.-i. Takehiro et al. (2024). This is due to a monotonically increasing Rhines scale and subsequent migration/merging of the jets. More work is needed to verify whether other state-of-the-art 3D simulations can achieve multiple high-latitude jets in a steady state.
2. There appear to be two distinct forms of PV: Q_z for the CZ and Q_r for the WL, arising physically from the distinct topologies of the two types of eddies. Inside the tangent cylinder (high latitudes), the appropriate PV is largely homogenized to form staircase-like structures and associated multiple jets. Correspondingly, the local jet width matches appropriate Rhines scale quite well at high latitudes. Outside the tangent cylinder (low latitudes), Q_z is only weakly homogenized in the CZ and the superrotation appears to result directly from Busse columns’ Reynolds stresses. The superrotation in the WL is an imprint of that in the CZ, driven by upward viscous/circulation burrowing.
3. An idealized WL (a stable layer atop the CZ) has a strong effect on the dynamics, significantly altering the transport of heat and subsequent thermal wind balance, thus forcing the jets away from cylindrical alignment. This effect is most pronounced in the WL itself, but is also relevant in the bulk of the CZ.

These conclusions have broad consequences for how the giant planets’ zonal flows might be studied in the future. Overall, our results suggest that the dynamics of high-latitude jets can continue to be analyzed using quasi-2D theories separately for the CZ (staircase structures in Q_z) and WL (staircase structures in Q_r). In that sense, there may be no real resolution to the “deep versus shallow driving” debate, because the two layers (each of which is driven by roughly equal amounts of energy flux) can independently produce multiple jets. However, the coupling between the CZ and WL is important, especially for the cylindrical alignment (or lack thereof) of the zonal flows. This is true even without the enhanced baroclinicity provided by equatorially concentrated heating by the Sun (which was excluded in our

work). Making progress on the fine structure of the high-latitude jets will thus likely require modeling both layers simultaneously.

At low latitudes, in the region of superrotation outside the tangent cylinder, there seems to be more physics than can be included in a simple quasi-2D framework. In the CZ, there is significant outward transport of angular momentum by the Reynolds stresses from outwardly flared Busse columns. PV (Q_z in this case) is only weakly homogenized across the superrotating jet, and thus the flare of the Busse columns seems to be essential for the generation of superrotation. What remains unclear is whether this same outward flare would be reproduced in quasi-2D simulations on the disc incorporating the topographic β -effect, i.e., whether the two mechanisms of homogenization of Q_z (in the presence of a negative β_{topo}) and the outward angular momentum transport by Busse columns are, in fact, equivalent outside the tangent cylinder. The first investigations of the topographic β -effect in 2D (Y. Zeng et al. 2025) did consistently yield superrotation, but the possible connection between negative β_{topo} and flared Busse columns was not explored.

Finally, we believe that our results on jet migration have laid bare a potential problem in current state-of-the-art 3D simulations of Jupiter’s jets, namely that the high-latitude jets in those models were very likely still evolving. Although it might be suspected that the introduction of a scale-independent Ekman-type drag to a rigid rotation rate (which has not been attempted in the global models, as far as we know) might stop this evolution, the problem then becomes determining the physical origins of such a drag. As far as we know, the CZ-only and CZ-WL cases presented in this work are the only fully equilibrated 3D simulations of multiple high-latitude jets that currently exist. The fact that our simulations only equilibrate only after $O(10)$ diffusion times leads us to speculate that most prior 3D simulations of multiple high-latitude jets were analyzing a transient state. It would thus appear to remain a mystery how Jupiter achieves multiple high-latitude *steady* jets.

ACKNOWLEDGMENTS

We thank P. Wulff, A. van Kan, N. Lewis, P. Marcus, E. Knobloch, H. Quan, W. Kang, G. Flierl, S. Tobias, Y. Kaspi, and J. Pedlosky for helpful discussions. This work was primarily supported by L. Matilsky’s NSF Astronomy & Astrophysics Postdoctoral Fellowship award AST-2202253 and the COFFIES DRIVE Science Center (NASA grant 80NSSC22M0162), with

additional support from NASA grants 80NSSC18K1127 and 80NSSC24K0125. M. Browning was supported by the UK Science and Technology Facilities Council under grant agreement ST/Y0021561/1. Part of this work was performed during the the Woods Hole Oceanographic Institution's Geophysical Fluid Dynamics Programs of 2024 and 2025, which were funded by the National Science Foundation grant OCE-1829864. Computational resources were provided by the NASA High-

End Computing (HEC) Program through the NASA Advanced Supercomputing (NAS) Division at Ames Research Center. `Rayleigh` is supported by the Computational Infrastructure for Geodynamics (CIG) through NSF awards NSF-0949446 and NSF-1550901. For reproducibility, the `Rayleigh` input files and final checkpoints for each simulation are publicly accessible at <https://doi.org/10.5281/zenodo.20332552>

APPENDIX

A. BACKGROUND STATE

Here we describe how the background state of the CZ–WL case is constructed in the radius range $r = (r_{\text{in}}, r_{\text{out}})$. (The CZ-only case is the same, but considers only the radius range $r = (r_{\text{in}}, r_c)$.) The implementation is similar to the solar simulations of L. I. Matilsky & J. Toomre (2021); L. I. Matilsky et al. (2022, 2024, 2025, 2026), except now the stable layer (the WL) is above the CZ instead of below it.

In terms of the dimensional background state, the perfect gas law is

$$\tilde{p}^* = \left[\frac{(\gamma - 1)c_p}{\gamma} \right] \tilde{\rho}^* \tilde{T}^*, \quad (\text{A1})$$

hydrostatic balance is

$$\frac{d\tilde{p}^*}{dr^*} = -\tilde{\rho}^* \tilde{g}^*, \quad (\text{A2})$$

and the first law of thermodynamics is

$$\frac{1}{c_p} \left(\frac{d\tilde{s}}{dr} \right)^* = \frac{d \ln \tilde{T}^*}{dr^*} - \left(\frac{\gamma - 1}{\gamma} \right) \frac{d \ln \tilde{\rho}^*}{dr^*}. \quad (\text{A3})$$

After the nondimensionalization described in Section 2.3, Equations (A1)–(A3) take the form

$$\tilde{p} = \tilde{\rho} \tilde{T}, \quad (\text{A4})$$

$$\frac{d\tilde{p}}{dr} = -\text{Di} \left(\frac{\gamma}{\gamma - 1} \right) \tilde{\rho} \tilde{g}, \quad (\text{A5})$$

and

$$\frac{d\tilde{s}}{dr} = \frac{1}{\gamma} \frac{d \ln \tilde{T}}{dr} - \left(\frac{\gamma - 1}{\gamma} \right) \frac{d \ln \tilde{\rho}}{dr}, \quad (\text{A6})$$

where $\tilde{s} := \tilde{s}^*/c_p$ and $\tilde{p} := \tilde{p}^*/p_{\text{cz}}$. Recall that $\text{Di} := g_{\text{cz}}H/c_p T_{\text{cz}}$ (Equation 22). We combine Equations (A4)–(A6) to find

$$\frac{d\tilde{T}}{dr} - \left(\frac{d\tilde{s}}{dr} \right) \tilde{T} = -\text{Di} \tilde{g}, \quad (\text{A7})$$

which has the exact solution

$$\tilde{T} = e^{\tilde{s}} \left[\tilde{T}(r_{\text{in}}) - \text{Di} \int_{r_{\text{in}}}^r \tilde{g}(x) e^{-\tilde{s}(x)} dx \right]. \quad (\text{A8})$$

Note that the actual background entropy \tilde{s} is only relevant up to an integration constant. In Equation (A8), we have therefore chosen, without loss of generality,

$$\tilde{s}(r) := \int_{r_{\text{in}}}^r \frac{d\tilde{s}}{dr'} dr' \quad (\text{A9})$$

such that $\tilde{s} \equiv 0$ in the CZ.

We then eliminate \tilde{p} from Equations (A4) and (A5) to yield

$$\tilde{\rho} = \tilde{\rho}(r_{\text{in}}) \exp \left[- \left(\frac{\gamma}{\gamma - 1} \right) \tilde{s} \right] \tilde{T}^{1/(\gamma-1)}. \quad (\text{A10})$$

For $\tilde{g}(r) \propto 1/r^2$ and the normalization condition $(4\pi/V_{\text{cz}}) \int_{r_c}^{r_{\text{out}}} \tilde{g}(r) r^2 dr = 1$ (where $V_{\text{cz}} := (4\pi/3)(r_{\text{out}}^3 - r_c^3) = (4\pi/3)[(1 - \alpha_{\text{cz}}^3)/(1 - \alpha_{\text{cz}})^3]$ is the nondimensional volume of the CZ), we require

$$\tilde{g}(r) = \left[\frac{1 - \alpha_{\text{cz}}^3}{3(1 - \alpha_{\text{cz}})^3} \right] \frac{1}{r^2}. \quad (\text{A11})$$

To model the transition from convective instability to stability at $r = r_c$, we choose $d\tilde{s}/dr$ to be $\equiv 0$ in the CZ, $\equiv 1$ in the WL, and continuously matched in between over the distance $\delta = 0.05$. We accomplish this via quartic matching:

$$\frac{d\tilde{s}}{dr} = \begin{cases} 0 & r \leq r_c \\ 1 - \left[1 - \left(\frac{r - r_c}{\delta} \right)^2 \right]^2 & r_c < r < r_c + \delta \\ 1 & r \geq r_c + \delta. \end{cases} \quad (\text{A12})$$

Note that the amplitude of $d\tilde{s}/dr$ in the WL is technically arbitrary and choosing $d\tilde{s}/dr \equiv 1$ is really another way to specify N_{ρ}^{w1} , given Equations (A8)–(A10).

There are three equations relating $\tilde{\rho}(r_{\text{in}})$, $\tilde{T}(r_{\text{in}})$, Di, γ , α_{cz} , and N_{ρ}^{cz} : two from our choice of nondimensionalization— $(4\pi/V_{\text{cz}})\int_{r_c}^{r_{\text{out}}}\tilde{\rho}(r)r^2dr = 1$ and $(4\pi/V_{\text{cz}})\int_{r_c}^{r_{\text{out}}}\tilde{T}(r)r^2dr = 1$ —and one from the definition $N_{\rho}^{\text{cz}} := \ln[\tilde{\rho}(r_{\text{in}})/\tilde{\rho}(r_c)]$. Thus, $\tilde{\rho}(r_{\text{in}})$, $\tilde{T}(r_{\text{in}})$, and Di may all be regarded as functions of γ , α_{cz} , and N_{ρ}^{cz} .

Because $d\tilde{s}/dr \equiv 0$ in the CZ, explicit formulae can be derived for Di and $\tilde{T}(r_c)$:

$$\text{Di} := \frac{g_{\text{cz}}H}{c_p T_{\text{cz}}} = \frac{3\alpha_{\text{cz}}(1 - \alpha_{\text{cz}})^2(1 - e^{-N_{\rho}^{\text{cz}}/n})}{\frac{3\alpha_{\text{cz}}}{2}(1 - \alpha_{\text{cz}}^2)(1 - e^{-N_{\rho}^{\text{cz}}/n}) - (1 - \alpha_{\text{cz}}^3)(\alpha_{\text{cz}} - e^{-N_{\rho}^{\text{cz}}/n})} \quad (\text{A13})$$

and

$$\tilde{T}(r_c) = \frac{(1 - \alpha_{\text{cz}}^3)(1 - \alpha_{\text{cz}})}{\frac{3\alpha_{\text{cz}}}{2}(1 - \alpha_{\text{cz}}^2)(1 - e^{-N_{\rho}^{\text{cz}}/n}) - (1 - \alpha_{\text{cz}}^3)(\alpha_{\text{cz}} - e^{-N_{\rho}^{\text{cz}}/n})}, \quad (\text{A14})$$

where

$$n := \frac{1}{\gamma - 1} = 2 \quad (\text{A15})$$

is the ‘‘polytropic index’’ (but note that only the convective zone has the polytropic stratification $\tilde{\rho} = \tilde{T}^2$). The equation for $\tilde{\rho}(r_c)$ is transcendental and requires a numerical solution. For the cases considered here, note that $\text{Di} = 0.599$, $\tilde{T}(r_{\text{in}}) = 1.35$, and $\tilde{\rho}(r_{\text{in}}) = 1.77$.

The background $\tilde{\rho}(r)$ and $\tilde{T}(r)$ are now completely determined via Equations (A8)–(A15) and the control parameters γ , α_{cz} , N_{ρ}^{cz} , and (for the CZ–WL case) α_{wl} and N_{ρ}^{wl} .

The background heating \tilde{Q} is chosen to input a heating layer at the base of the CZ and a cooling layer at the top of the CZ, each of width $\delta_Q = 0.1$. This is accomplished again via quartics.

$$\tilde{Q} = \begin{cases} A B_1 \left[1 - \left(\frac{r - r_{\text{in}}}{\delta_Q} \right)^2 \right]^2 & r \leq r_{\text{in}} + \delta_Q \\ -A B_2 \left[1 - \left(\frac{r - r_c}{\delta_Q} \right)^2 \right]^2 & r_c - \delta_Q \leq r \leq r_c \\ 0 & \text{otherwise} \end{cases} \quad (\text{A16})$$

For the CZ–WL case, we also multiply the expression in Equation (A16) by $[1 + \tanh((r - r_c)/0.005)]/2$ to ensure that the transition to $\tilde{Q} \equiv 0$ in the WL is not completely

abrupt. The coefficients B_1 and B_2 are chosen such that the energy injected by the heating layer is exactly removed by the cooling layer, i.e.,

$$4\pi \int_{r_{\text{in}}}^{r_c} \tilde{Q}(r')r'^2 dr' = 0. \quad (\text{A17})$$

Since $\tilde{Q}^* = (F_{\text{cz}}/H)\tilde{Q}$, $\tilde{F}^* = F_{\text{cz}}\tilde{F}$, and $\tilde{F}^* := (H/r^2)\int_r^{r_{\text{out}}}\tilde{Q}^*(r')r'^2 dr'$ (recall Equation (11)), normalization of the heat flux (i.e., $(4\pi/V_{\text{cz}})\int_{r_c}^{r_{\text{out}}}\tilde{F}(r)r^2 dr = 1$) requires that

$$\frac{4\pi}{V_{\text{cz}}} \int_{r_{\text{in}}}^{r_c} \int_r^{r_c} \tilde{Q}(r')r'^2 dr' dr = 1, \quad (\text{A18})$$

which sets the proportionality constant A in Equation (A16).

B. REDIMENSIONALIZATION OF THE SIMULATIONS

Although we report all results in nondimensional units in this work, we can always consider dimensional analogs of the simulations to more easily compare with observations and prior work, a process we call redimensionalization. Because there are many more dimensional parameters than nondimensional ones, each nondimensional simulation corresponds to an infinite number of dimensional analogs (see L. I. Matilsky et al. 2026, their Appendix E, for more details). To choose a particular analog, we arbitrarily set the parameters Ω_0 , H , and ρ_{cz} to Jovian-like values. This forces us to choose a non-Jovian-like value for the energy flux F_{cz} driving the convection:

$$F_{\text{cz}} = \frac{\text{Ra}_f \text{Ek}^3}{\text{Pr}^2 \text{Di}} \rho_{\text{cz}} (2\Omega_0 H)^3, \quad (\text{B19})$$

which ends up being much higher than the 7.5 W m^{-2} expected for Jupiter. We are also forced to unrealistically high values for the dimensional diffusivities ν_{cz} and κ_{cz} .

Our adopted dimensional values, corresponding cgs units for the fluid variables, and associated dimensional timescales, are shown in Table B1. To use this table, simply multiply the reported nondimensional values in the simulation by the corresponding nondimensional cgs unit. For instance, because $[\mathbf{u}] = 4.8 \times 10^3 \text{ m s}^{-1}$, the superrotation velocities shown in Figure 5 have amplitudes of about $0.08[\mathbf{u}] = 380 \text{ m s}^{-1}$ (for the CZ-only case) and $0.13[\mathbf{u}] = 620 \text{ m s}^{-1}$ (for the CZ–WL case).

Table B1. Redimensionalization parameters for our simulations. The density ρ_{cz} was adopted from [M. French et al. \(2012\)](#) and corresponds to the value at $0.9a$. We choose $a = 70,000$ km and $\Omega_0 = 1.8 \times 10^{-4}$ rad s $^{-1}$ (corresponding to a Jovian sidereal day of $2\pi/\Omega_0 = 9.9$ hr) as standard Jovian values. Note that the dimensions of the torque densities in [Figure 15](#) are the same as the unit of kinetic energy density $[\tilde{\rho}\mathbf{u}^2/2]$.

Parameter	Source	Value
d	a/r_{out}	13,000 km
Ω_0	standard	1.8×10^{-4} rad s $^{-1}$
N_{wl}	$2\Omega_0\sqrt{\text{Bu}}$	1.5×10^{-3} rad s $^{-1}$
F_{cz}	Equation (B19)	3.3×10^8 W m $^{-2}$
ν_{cz}	$\text{Ek}(2\Omega_0 H^2)$	2.9×10^{10} cm 2 s $^{-1}$
κ_{cz}	$(\text{Ek}/\text{Pr})(2\Omega_0 H^2)$	5.7×10^{10} cm 2 s $^{-1}$
ρ_{cz}	M. French et al. (2012)	0.5 g cm $^{-3}$
$[\mathbf{u}]$	$2\Omega_0 H$	4.8×10^3 m s $^{-1}$
$[\tilde{\rho}\mathbf{u}^2/2]$	$\rho_{cz}(2\Omega_0 H)^2$	1.2×10^{11} erg cm $^{-3}$
$[Q_z]$	$2\Omega_0/H$	2.7×10^{-13} s $^{-1}$ cm $^{-1}$
$[\tilde{\rho}\mathbf{u}]$	$\rho_{cz}(2\Omega_0)H$	2.4×10^3 g $^{-1}$ cm $^{-2}$ s $^{-1}$
$[\partial \langle u_\phi \rangle^2 / \partial z]$	$(2\Omega_0)^2 H$	1.7×10^{-2} cm s $^{-2}$
$[\tilde{\rho}\lambda \langle u_\phi \rangle]$	$\rho_{cz}(2\Omega_0)H^2$	3.2×10^{12} g cm $^{-1}$ s $^{-1}$
$[t]$ (dimensional time unit)	$(2\Omega_0)^{-1}$	0.77 hr
expected eddy turnover time	$[t]/\text{Ro}_c$	3.9 hr
expected buoyancy time	$[t]/\sqrt{\text{Bu}}$	0.19 hr
viscous diffusion time	H^2/ν_{cz}	2.0 yr
thermal diffusion time	H^2/κ_{cz}	1.0 yr

REFERENCES

- Brogi, M., Kok, R. J. d., Albrecht, S., et al. 2016, *Astrophys. J.*, 817, 106, doi: [10.3847/0004-637x/817/2/106](#)
- Brummell, N. H., & Hart, J. E. 1993, *Geophys. Astrophys. Fluid Dyn.*, 68, 85–114, doi: [10.1080/03091929308203563](#)
- Brun, A. S., Strugarek, A., Varela, J., et al. 2017, *Astrophys. J.*, 836, 192, doi: [10.3847/1538-4357/aa5c40](#)
- Busse, F. H. 2002, *Phys. Fluids*, 14, 1301, doi: [10.1063/1.1455626](#)
- Camisassa, M. E., & Featherstone, N. A. 2022, *Astrophys. J.*, 938, 65, doi: [10.3847/1538-4357/ac879f](#)
- Cho, J. Y.-K., & Polvani, L. M. 1996, *Phys. Fluids*, 8, 1531–1552, doi: [10.1063/1.868929](#)
- Clark, A. 1973, *J. Fluid Mech.*, 60, 561, doi: [10.1017/s0022112073000340](#)
- Clune, T., Elliott, J., Miesch, M., Toomre, J., & Glatzmaier, G. 1999, *Par. Comp.*, 25, 361, doi: [10.1016/s0167-8191\(99\)00009-5](#)
- Dickinson, R. E. 1969, *J. Atm. Sci.*, 26, 73–81, doi: [10.1175/1520-0469\(1969\)026<0073:topwzf>2.0.co;2](#)
- Duer, K., Gavriel, N., Galanti, E., et al. 2021, *Geophys. Res. Lett.*, 48, doi: [10.1029/2021gl095651](#)
- Ertel, H. 1942, *Met. Zeit.*, 59, 277
- Featherstone, N. A., Edelmann, P. V. F., Gassmoeller, R., Matilsky, L. I., & Wilson, C. R. 2024, doi: [10.5281/ZENODO.11391213](#)
- Featherstone, N. A., & Hindman, B. W. 2016, *Astrophys. J.*, 818, 32, doi: [10.3847/0004-637x/818/1/32](#)
- Fletcher, L. N., Kaspi, Y., Guillot, T., & Showman, A. P. 2020, *Space Sci. Rev.*, 216, doi: [10.1007/s11214-019-0631-9](#)
- French, M., Becker, A., Lorenzen, W., et al. 2012, *Astrophys. J. Supp.*, 202, 5, doi: [10.1088/0067-0049/202/1/5](#)
- Galanti, E., & Kaspi, Y. 2020, *Mon. Not. R. Astron. Soc.*, 501, 2352–2362, doi: [10.1093/mnras/staa3722](#)
- Gastine, T., & Wicht, J. 2012, *Icar.*, 219, 428, doi: [10.1016/j.icarus.2012.03.018](#)
- Gastine, T., Wicht, J., & Aurnou, J. 2013, *Icar.*, 225, 156, doi: [10.1016/j.icarus.2013.02.031](#)
- Gilman, P. A. 1972, *Sol. Phys.*, 27, 3, doi: [10.1007/bf00151765](#)
- Gilman, P. A., & Glatzmaier, G. A. 1981, *Astrophys. J. Supp.*, 45, 335, doi: [10.1086/190714](#)
- Gough, D. O. 1969, *J. Atm. Sci.*, 26, 448, doi: [10.1175/1520-0469\(1969\)026<0448:taafc>2.0.co;2](#)
- Greer, B. J., Hindman, B. W., & Toomre, J. 2016, *Astrophys. J.*, 824, 4, doi: [10.3847/0004-637x/824/1/4](#)

- Guillot, T. 2005, *Ann. Rev. Earth Plan. Sci.*, 33, 493–530, doi: [10.1146/annurev.earth.32.101802.120325](https://doi.org/10.1146/annurev.earth.32.101802.120325)
- Hadjerci, G., Bouillaut, V., Miquel, B., & Gallet, B. 2024, *J. Fluid Mech.*, 998, doi: [10.1017/jfm.2024.556](https://doi.org/10.1017/jfm.2024.556)
- Hanasoge, S. M., Duvall, T. L., & Sreenivasan, K. R. 2012, *Proc. Nat. Acad. Sci.*, 109, 11928, doi: [10.1073/pnas.1206570109](https://doi.org/10.1073/pnas.1206570109)
- Haurwitz, B. 1940, *J. Mar. Res.*, 3, 254–267
- Heimpel, M., Gastine, T., & Wicht, J. 2015, *Nat. Geosci.*, 9, 19–23, doi: [10.1038/ngeo2601](https://doi.org/10.1038/ngeo2601)
- Heimpel, M. H., Yadav, R. K., Featherstone, N. A., & Aurnou, J. M. 2022, *Icar.*, 379, 114942, doi: [10.1016/j.icarus.2022.114942](https://doi.org/10.1016/j.icarus.2022.114942)
- Heng, K., & Showman, A. P. 2015, *Ann. Rev. Earth Plan. Sci.*, 43, 509–540, doi: [10.1146/annurev-earth-060614-105146](https://doi.org/10.1146/annurev-earth-060614-105146)
- Howe, R. 2009, *Liv. Rev. Sol. Phys.*, 6, 1, doi: [10.12942/lrsp-2009-1](https://doi.org/10.12942/lrsp-2009-1)
- Imamura, T., Mitchell, J., Lebonnois, S., et al. 2020, *Space Sci. Rev.*, 216, doi: [10.1007/s11214-020-00703-9](https://doi.org/10.1007/s11214-020-00703-9)
- Ingersoll, A. P., Dowling, T. E., Gierasch, P. J., et al. 2004, *Dynamics of Jupiter's atmosphere*, Vol. 105 (Cambridge University Press, Cambridge, UK)
- Jones, C., Boronski, P., Brun, A., et al. 2011, *Icar.*, 216, 120, doi: [10.1016/j.icarus.2011.08.014](https://doi.org/10.1016/j.icarus.2011.08.014)
- Joshi-Hartley, T., Browning, M. K., Currie, L. K., et al. 2025, *Mon. Not. R. Astron. Soc.*, 541, 2291–2303, doi: [10.1093/mnras/staf1131](https://doi.org/10.1093/mnras/staf1131)
- Kaspi, Y., Galanti, E., Showman, A. P., et al. 2020, *Space Sci. Rev.*, 216, doi: [10.1007/s11214-020-00705-7](https://doi.org/10.1007/s11214-020-00705-7)
- Kaspi, Y., Galanti, E., Park, R. S., et al. 2023, *Nat. Astron.*, 7, 1463–1472, doi: [10.1038/s41550-023-02077-8](https://doi.org/10.1038/s41550-023-02077-8)
- Knutson, H. A., Charbonneau, D., Allen, L. E., et al. 2007, *Nat.*, 447, 183–186, doi: [10.1038/nature05782](https://doi.org/10.1038/nature05782)
- Kraichnan, R. H. 1967, *Phys. Fluids*, 10, 1417–1423, doi: [10.1063/1.1762301](https://doi.org/10.1063/1.1762301)
- Lewis, N. T., Joshi-Hartley, T., Tobias, S. M., Currie, L. K., & Browning, M. K. 2026, *Astrophys. J.*, 998, 52, doi: [10.3847/1538-4357/ae2ea8](https://doi.org/10.3847/1538-4357/ae2ea8)
- Li, J. 2018, *Astrophys. J.*, 867, 89, doi: [10.3847/1538-4357/aae31a](https://doi.org/10.3847/1538-4357/aae31a)
- Lian, Y., & Showman, A. P. 2008, *Icar.*, 194, 597–615, doi: [10.1016/j.icarus.2007.10.014](https://doi.org/10.1016/j.icarus.2007.10.014)
- Lindal, G. F., Wood, G. E., Levy, G. S., et al. 1981, *J. Geophys. Res. Space Phys.*, 86, 8721–8727, doi: [10.1029/ja086ia10p08721](https://doi.org/10.1029/ja086ia10p08721)
- Lorenz, E. N. 1972, *J. Atm. Sci.*, 29, 258–265, doi: [10.1175/1520-0469\(1972\)029<0258:biorwm>2.0.co;2](https://doi.org/10.1175/1520-0469(1972)029<0258:biorwm>2.0.co;2)
- Maltrud, M. E., & Vallis, G. K. 1991, *J. Fluid Mech.*, 228, 321–342, doi: [10.1017/s0022112091002720](https://doi.org/10.1017/s0022112091002720)
- Marcus, P. S. 1988, *Nat.*, 331, 693–696, doi: [10.1038/331693a0](https://doi.org/10.1038/331693a0)
- Matilsky, L. I. 2023, *Mon. Not. R. Astron. Soc. Lett.*, 526, L100–L104, doi: [10.1093/mnrasl/slad121](https://doi.org/10.1093/mnrasl/slad121)
- Matilsky, L. I., Brummell, N. H., Hindman, B. W., & Toomre, J. 2024, *Astrophys. J.*, 962, 189, doi: [10.3847/1538-4357/ad18b2](https://doi.org/10.3847/1538-4357/ad18b2)
- Matilsky, L. I., Hindman, B. W., Featherstone, N. A., Blume, C. C., & Toomre, J. 2022, *Astrophys. J. Lett.*, 940, L50, doi: [10.3847/2041-8213/ac93ef](https://doi.org/10.3847/2041-8213/ac93ef)
- Matilsky, L. I., Korre, L., & Brummell, N. H. 2025, *Astrophys. J. Lett.*, 991, L1, doi: [10.3847/2041-8213/ade3](https://doi.org/10.3847/2041-8213/ade3)
- Matilsky, L. I., Korre, L., & Brummell, N. H. 2026, *Astrophys. J.*, doi: [10.48550/ARXIV.2601.11943](https://doi.org/10.48550/ARXIV.2601.11943)
- Matilsky, L. I., & Toomre, J. 2021, in *20.5th Cambridge Workshop on Cool Stars, Stellar Systems, and the Sun*, ed. S. J. Wolk (Zenodo), doi: [10.5281/ZENODO.4750777](https://doi.org/10.5281/ZENODO.4750777)
- Matsui, H., Heien, E., Aubert, J., et al. 2016, *Geochem., Geophys., Geosys.*, 17, 1586, doi: [10.1002/2015gc006159](https://doi.org/10.1002/2015gc006159)
- Medvedev, A. S., Kuroda, T., & Hartogh, P. 2011, *Aeo. Res.*, 3, 145–156, doi: [10.1016/j.aeolia.2011.05.001](https://doi.org/10.1016/j.aeolia.2011.05.001)
- Morin, V., & Dormy, E. 2006, *Phys. Fluids*, 18, doi: [10.1063/1.2215605](https://doi.org/10.1063/1.2215605)
- Nicolas, Q., & Vallis, G. K. 2026, *Plan. Sci. J.*, 7, 98, doi: [10.3847/psj/ae5c96](https://doi.org/10.3847/psj/ae5c96)
- Ogura, Y., & Phillips, N. A. 1962, *J. Atm. Sci.*, 19, 173, doi: [10.1175/1520-0469\(1962\)019<0173:saodas>2.0.co;2](https://doi.org/10.1175/1520-0469(1962)019<0173:saodas>2.0.co;2)
- Parker, E. N. 1993, *Astrophys. J.*, 408, 707, doi: [10.1086/172631](https://doi.org/10.1086/172631)
- Pedlosky, J. 1987, *Geophysical Fluid Dynamics* (New York: Springer), doi: [10.1007/978-1-4612-4650-3](https://doi.org/10.1007/978-1-4612-4650-3)
- Read, P. L., & Lebonnois, S. 2018, *Ann. Rev. Earth Plan. Sci.*, 46, 175–202, doi: [10.1146/annurev-earth-082517-010137](https://doi.org/10.1146/annurev-earth-082517-010137)
- Rhines, P. B. 1975, *J. Fluid Mech.*, 69, 417–443, doi: [10.1017/s0022112075001504](https://doi.org/10.1017/s0022112075001504)
- Roberts, P. H., & Glatzmaier, G. A. 2000, *Rev. Mod. Phys.*, 72, 1081–1123, doi: [10.1103/revmodphys.72.1081](https://doi.org/10.1103/revmodphys.72.1081)
- Rossby, C.-G. 1936, *Dynamics of steady ocean currents in the light of experimental fluid mechanics*, *Papers in Physical Oceanography and Meteorology* (Massachusetts Institute of Technology and Woods Hole Oceanographic Institution)
- Rossby, C.-G. 1939, *J. Mar. Res.*, 2, 38
- Saito, I., & Ishioka, K. 2015, *J. Atm. Sci.*, 72, 1466–1483, doi: [10.1175/jas-d-14-0235.1](https://doi.org/10.1175/jas-d-14-0235.1)
- Schubert, W. H., Taft, R. K., & Silvers, L. G. 2009, *J. Adv. Mod. Earth Sys.*, 1, doi: [10.3894/james.2009.1.2](https://doi.org/10.3894/james.2009.1.2)

- Scott, R. K., & Polvani, L. M. 2007, *J. Atm. Sci.*, 64, 3158–3176, doi: [10.1175/jas4003.1](https://doi.org/10.1175/jas4003.1)
- Scott, R. K., & Polvani, L. M. 2008, *Geophys. Res. Lett.*, 35, doi: [10.1029/2008gl036060](https://doi.org/10.1029/2008gl036060)
- Seiff, A., Kirk, D. B., Knight, T. C. D., et al. 1996, *Sci.*, 272, 844–845, doi: [10.1126/science.272.5263.844](https://doi.org/10.1126/science.272.5263.844)
- Showman, A. P. 2007, *J. Atm. Sci.*, 64, 3132–3157, doi: [10.1175/jas4007.1](https://doi.org/10.1175/jas4007.1)
- Song, X., & Yang, J. 2021, *Front. Astron. Space Sci.*, 8, doi: [10.3389/fspas.2021.708023](https://doi.org/10.3389/fspas.2021.708023)
- Soyuer, D., Neuenschwander, B., & Helled, R. 2022, *Astron. J.*, 165, 27, doi: [10.3847/1538-3881/aca08d](https://doi.org/10.3847/1538-3881/aca08d)
- Spiegel, E. A., & Zahn, J.-P. 1992, *Astron. Astrophys.*, 265, 106
- Takehiro, S.-i., Sasaki, Y., Ishioka, K., et al. 2024, *Icar.*, 420, 116154, doi: [10.1016/j.icarus.2024.116154](https://doi.org/10.1016/j.icarus.2024.116154)
- Vallis, G. K. 2017, *Atmospheric and Oceanic Fluid Dynamics: Fundamentals and Large-Scale Circulation*, 2nd edn. (Cambridge University Press), doi: [10.1017/9781107588417](https://doi.org/10.1017/9781107588417)
- Vallis, G. K., & Maltrud, M. E. 1993, *J. Phys. Oceaen.*, 23, 1346–1362, doi: [10.1175/1520-0485\(1993\)023<1346:gomfaj>2.0.co;2](https://doi.org/10.1175/1520-0485(1993)023<1346:gomfaj>2.0.co;2)
- Vallis, G. K., Matilsky, L. I., & Nicolas, Q. 2026, *Phil. Trans. R. Soc. A*, In press
- Warneford, E. S., & Dellar, P. J. 2017, *J. Fluid Mech.*, 822, 484–511, doi: [10.1017/jfm.2017.232](https://doi.org/10.1017/jfm.2017.232)
- Williams, G. P. 1978, *J. Atm. Sci.*, 35, 1399–1426, doi: [10.1175/1520-0469\(1978\)035<1399:pcbroy>2.0.co;2](https://doi.org/10.1175/1520-0469(1978)035<1399:pcbroy>2.0.co;2)
- Williams, G. P. 2002, *J. Atm. Sci.*, 59, 1356–1370, doi: [10.1175/1520-0469\(2002\)059<1356:jdpitg>2.0.co;2](https://doi.org/10.1175/1520-0469(2002)059<1356:jdpitg>2.0.co;2)
- Wulff, P. N., Dietrich, W., Christensen, U. R., & Wicht, J. 2022, *Mon. Not. R. Astron. Soc.*, 517, 5584–5593, doi: [10.1093/mnras/stac3045](https://doi.org/10.1093/mnras/stac3045)
- Yamazaki, Y., Read, P., & Skeet, D. 2005, *Plan. Space Sci.*, 53, 508–525, doi: [10.1016/j.pss.2004.03.009](https://doi.org/10.1016/j.pss.2004.03.009)
- Zeng, Y., Kang, W., Flierl, G. R., & Vallis, G. K. 2025, *Proceedings of the National Academy of Sciences*, arXiv:2503.17828, doi: [10.48550/arXiv.2503.17828](https://doi.org/10.48550/arXiv.2503.17828)